

Strut-Based Cellular to Shellular Funicular Materials

Mostafa Akbari, Armin Mirabolghasemi, Mohammad Bolhassani,
Abdolhamid Akbarzadeh,* and Masoud Akbarzadeh*

Owing to the fact that effective properties of low-density cellular solids heavily rely on their underlying architecture, a variety of explicit and implicit techniques exists for designing cellular geometries. However, most of these techniques fail to present a correlation among architecture, internal forces, and effective properties. This paper introduces an alternative design strategy based on the static equilibrium of forces, equilibrium of polyhedral frames, and reciprocity of form and force. This novel approach reveals a geometric relationship among the truss system architecture, topological dual, and equilibrium of forces on the basis of 3D graphic statics. This technique is adapted to devise periodic strut-based cellular architectures under certain boundary conditions and they are manipulated to construct shell-based (shellular) cells with a variety of mechanical properties. By treating the materialized unit cells as representative volume elements (RVE), multiscale homogenization is used to investigate their effective linear elastic properties. Validated by experimental tests on 3D printed funicular materials, it is shown that by manipulating the RVE topology using the proposed methodology, alternative strut materialization schemes, and rational addition of bracing struts, cellular mechanical metamaterials can be systematically architected to demonstrate properties ranging from bending- to stretching-dominated, realize metafluidic behavior, or create novel hybrid shellulars.

packed together to fill a predefined space. Their growing range of utilization spans over numerous applications, such as light-weight load-bearing structures, energy absorbers, tissue scaffolds, heat transfer, and batteries, to name a few.^[1] Developing unit cells, tessellable in 2D- or 3D arrays, is a common approach for designing periodic cellular solids.^[2] Based on geometrical configurations of the unit cell, 3D cellular materials are typically classified as strut-, polyhedron-, and shell-based (shellular) architectures,^[3–5] even though a unit cell can be a hybrid of these classes.

Strut-based cellular materials comprise a network of slender members similar to the skeleton of a glass sponge in nature^[6]. Topologically, their unit cells include a group of vertices v_i and edges e_i in 3D space, where each vertex is connected to three or more edges (Figure 1b). Although the elasto-plastic behavior of the base solid material, struts geometry, and their configurations determine the structural performance of these cellular materials, their mechanical performance in compression is often governed by the local buckling of

their slender members particularly for cellular materials with low relative densities^[7].

Polyhedron-based cellular materials consist of interconnected membranes constructing closed cells, similar to the microarchitecture of the cork^[8] or the iris leaf.^[9] The topology of these materials consists of a group of cells c_j , faces f_j , edges e_j , and vertices v_j , in which each edge is connected to more than two faces, making

1. Introduction

1.1. Architecture of Cellular Materials

Cellular solids can be defined as an assembly of random or periodic cells, comprising straight/curved struts, flat/curved plates, and/or solid bulks that cannot be considered as struts or plates,


M. Akbari, M. Akbarzadeh
Polyhedral Structures Laboratory
Department of Architecture
Weitzman School of Design
University of Pennsylvania
Philadelphia, PA 19146, USA
E-mail: masouda@upenn.edu

A. Mirabolghasemi, A. H. Akbarzadeh
Advanced Multifunctional and Multiphysics Metamaterials Lab (AM³L)
Department of Bioresource Engineering
McGill University
Montreal, QC H9X 3V9, Canada
E-mail: hamid.akbarzadeh@mcgill.ca

M. Bolhassani
Spitzer School of Architecture
The City College of New York
New York City, NY 10031, USA

A. H. Akbarzadeh
Department of Mechanical Engineering
McGill University
Montreal, QC H3A 0C3, Canada

M. Akbarzadeh
General Robotic
Automation
Sensing and Perception (GRASP) Lab
School of Engineering and Applied Science
University of Pennsylvania
3330 Walnut St, PA 19104, Philadelphia

 The ORCID identification number(s) for the author(s) of this article can be found under <https://doi.org/10.1002/adfm.202109725>.

DOI: 10.1002/adfm.202109725

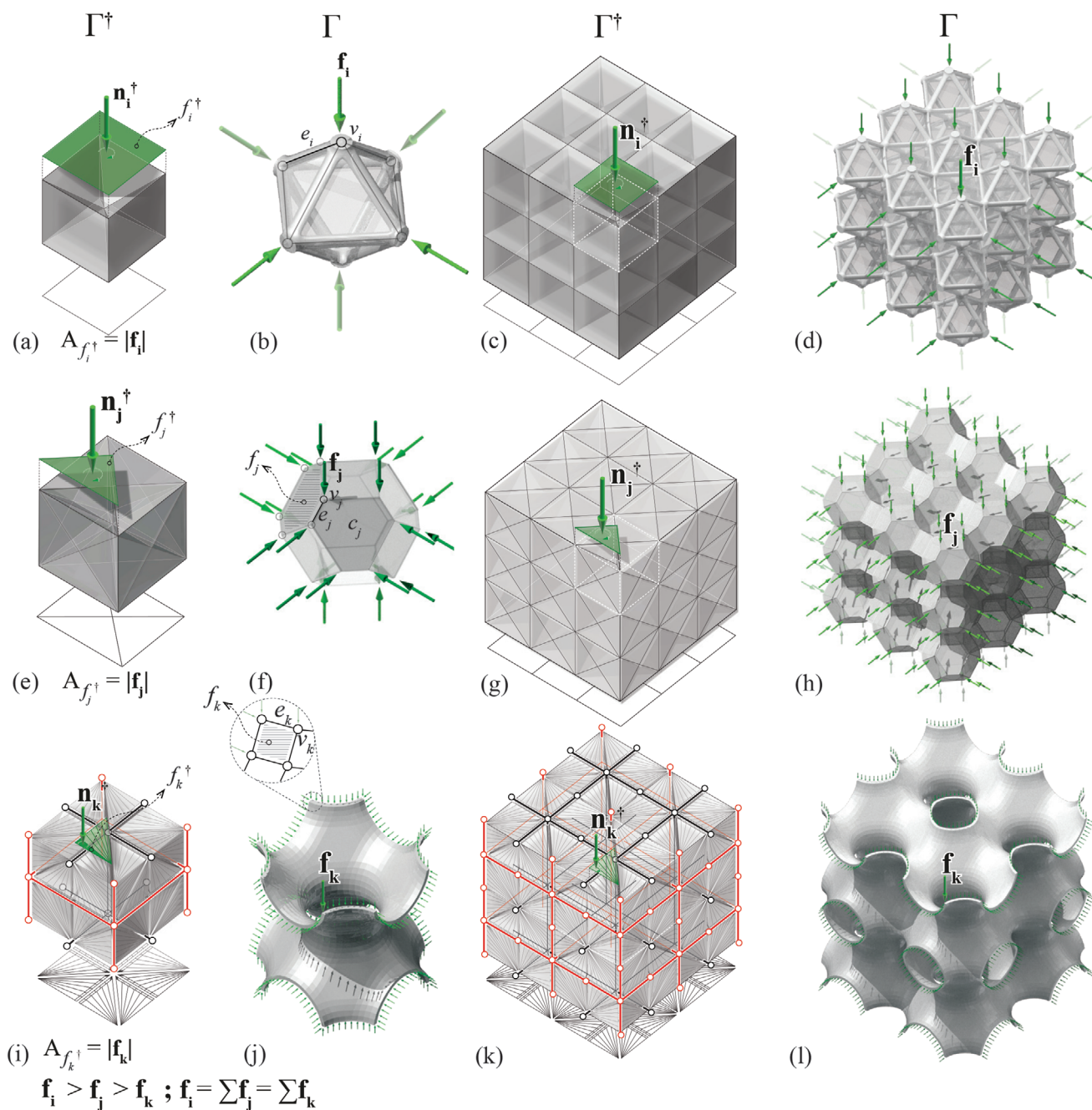


Figure 1. Simulating the architecture of different cellular materials in nature using PGS technique; the force and form diagrams of a strut-based cellular (a,b), a polyhedron cellular (e,f), and a shellular (i,j) unit-cell designed by PGS. The 3D aggregation of the force diagrams (c,g,k) results in different kinds of triply periodic cellular materials (d,h,l).

a non-manifold edge (Figure 1f).^[3] While the absence of interconnected pores puts forward this class of closed-cell cellular materials for thermal insulation and fluid barrier applications,^[3,4] it makes their additive manufacturing challenging for alternative resin- or powder-based 3D printing technologies.^[10,11]

Shellular materials as the third class of low-density materials are made up of cells comprising faces f_k , edges e_k , and vertices v_k . Compared to polyhedron cellular materials, each edge is adjacent to only two faces, making a two-manifold edge

(Figure 1j).^[12] By refining the discrete surface of these architectures, one can generate a continuous smooth-curved shell without self-intersection, the so-called shellular. Such geometries have been observed in natural materials (e.g., biological membranes, block polymers, and crystals^[3,13,14]) and divide the space into two sub-volumes. Although shellular materials can be based on any non-self-intersecting surface, they are routinely discussed together with triply periodic minimal surfaces (TPMS), a class of periodic intersection-free smooth surfaces

with zero mean curvature at each point (i.e., $H = (k_1 + k_2)/2 = 0$, in which k_1 and k_2 are the surface's principal curvatures) and minimum surface area for a given local boundary on the surface.^[15] Their presence in nature together with their properties have inspired researchers to make thin shells based on TPMSs and study their effective multifunctional properties.^[16–21] It has been shown that under a specific loading condition a TPMS shellular can display optimal stress distribution compared with its non-smooth counterpart.^[22] The shellular surface can also be perforated to impart programmable multistability and create deployable mechanical metamaterials.^[23]

The multifunctional properties of cellular materials are mainly governed by the architectural and topological features of their nano/micro/meso-structure and the force-flow within their elements rather than merely depending on the properties of their constituent materials.^[1,24] In fact, designing the architecture of cellular solids makes it possible to extend the property space of known materials, which can be visually demonstrated by 2D or 3D graphs, showing how their properties (e.g., density, Young's modulus, and yield stress) correlate with each other.^[25] As an example, by designing the architecture of nickel microlattices, researchers have extended the property space of nickel for low-range densities, elastic modulus, and strengths.^[1,26] Hence, to systematically enhance the material property space, it is essential to use a design methodology that can provide precise control over the geometry, topology, and force-flow within the system. The evident similarities between some cellular architectures with large-scale efficient structural systems motivated the authors to investigate the application of macro-scale structural design approaches for conceiving novel micro-scale cellular materials.

1.2. Stretching versus Bending Dominated Cellular Solids

Mechanical behavior of cellular materials under uni-axial tension spans from bending- to stretching-dominated; within the former, members mostly undergo bending and transversal loading, and sustain little to no axial loads, while the opposite holds true for the latter where most of the microstructure experiences axial tension/compression, resulting in a much higher stiffness/strength-to-weight ratios.^[3,16,27] Under this description, a cellular solid such as the simple cubic truss can act as stretching-dominated along one direction, while being bending-dominated along the others; nevertheless, the accepted definition generally includes any arbitrary tensile/compressive loading along any direction, rendering the simple cubic truss as a bending dominated lattice. Higher stiffness and strength of stretching-dominated cellular solids might suggest that they are more weight efficient; however, the structural efficiency is not limited to the concept of the maximum load per weight and instead is based on the specific performance requirement,^[28] which might include other functionalities such as mechanical unfeelability, acoustic, and auxetics properties that do not necessarily correspond to higher stiffness or strength. Consequently, stretching-dominated cellular materials are used as load-bearing structures, while bending-dominated cellular solids find potential applications in energy absorption and vibration insulation.^[29]

It has been shown that at small relative densities $\bar{\rho}$ (defined as the measured density ρ of a mono-material cellular solid divided by that of its constituent material ρ_s), mechanical properties such as effective moduli of stretching-dominated strut-based cellular materials correlate linearly with $\bar{\rho}$, whereas in the bending-dominated type, they decrease more rapidly as $\bar{\rho}$ lessens. For instance, the elastic modulus of 3D open-cell bending-dominated foams generally correlates with ρ^2 .^[9,27] As a result, the relationship between $\bar{\rho}$ and effective Young's modulus \bar{E} is often used as an indicator of the degree of stretching dominance of a cellular material: the closer to linear correlation, the more stretching-dominated.

1.3. Large-Scale Compression/Tension-Dominated Structural Systems

In large scale load-bearing structures, the concept of structural efficiency generally refers to the maximum allowable supported load over the structure's mass.^[28] Hence, compression/tension-dominant structures are worthy examples of structurally efficient systems at large scale. In such systems, the directions of the internal force-flow conform to the geometry of the structure members. These systems are called funicular structures. They are axially loaded structures designed for predefined boundary conditions, comprising external forces with specific directions and magnitudes.^[30] A similar phenomenon exists in the micro-scale internal structure of a spongy bone, a classical example where material follows the principal stress directions and forms a delicate lattice network of tiny interlaced.^[31] Finding these load paths or stress trajectories has been the basis of design methodologies for efficient structural forms, which are often being referred as structural form finding techniques. The Sagrada Familia is an excellent example of using such forms in design and engineering. Antoni Gaudi (1852–1926) used a tedious physical form-finding technique, based on Robert Hooke's (1635–1703) hanging chain model, to find a funicular form for his structures.^[32,33]

Advances in computer science and engineering have allowed the development of form-finding techniques such as physics simulation engines,^[34] particle-spring systems,^[35] force density methods,^[36] and dynamic relaxation^[37] to find an optimal geometry of the structure under the given loading conditions and substitute the physical form-finding techniques.^[38] Over the past 20 years, extensive research has been carried out on the development of methodologies to automatically generate these load paths in a continuum field following the actual flow of stresses. These studies are either based on the finite element analyses^[39,40] or discrete (ground truss) and continuum topology optimization algorithms.^[41,42]

1.4. Graphic Statics

One powerful method of structural design is called graphic statics (GS) that is based on pure geometry. Graphic statics originated in the predigital era and continued to be used and developed even today.^[43–50] In this method, the geometry of the structure is represented by a diagram called form, and the magnitude and equilibrium of forces are represented by

a diagram called force. In this article, the form and force diagrams are, respectively, denoted by Γ and Γ^\dagger (Figure 2a). These diagrams are reciprocal, that is, geometrically dependent and topologically dual; in 2D space, each node (along with the edges converging toward it) in the form has a dual polygon in the force diagram, and each edge in the form is perpendicular (or parallel) to an edge in the force diagram. The equilibrium of forces in each node in the form of the structure is represented by a closed polygon, and the magnitude of the force in each member of the structure is measured by the length of the corresponding edge in the force diagram (Figure 2a). As a result, changing one diagram affects the geometry of the other. Thus, a designer can explicitly control the magnitude of the forces and the architecture of a structural system simply by modifying its force diagram. The structures designed by GS-based methods are among the prominent examples of innovative and efficient usage of material; many eminent engineers and designers such as Guastavino, Maillart, Eiffel, and Nervi constantly used graphic statics in design of their masterpieces.^[51,52]

Since the nineteenth century, several methods have been developed to extend graphic statics to three dimensions including the Cremona method based on reciprocal (non-planar) polygonal diagrams^[44,48,53] and the works of Föppl based on projective geometry.^[54] There is a particular extension of graphic statics in three dimensions based on a publication by Rankine.^[45] In this method, which is called 3D graphical statics using reciprocal polyhedral diagrams or polyhedral graphic statics (PGS), the equilibrium of the forces in a single node is represented by a closed polyhedron or a polyhedral cell with planar faces (Figure 2b).^[55–58] PGS allows design and exploration of spatial funicular polyhedral systems which are not feasible using the conventional methods of graphic statics. The authors of this paper explore here a potential application of this method in the design of cellular solids.

The geometry of funicular structures can be found using form finding methods based on two important theoretical assumptions: 1) Designed and the real boundary conditions should match (including the external loads and the supports' locations). Accordingly, a large-scale load-bearing structure, which is designed using these techniques, is stretching-/compression-dominated, only under the specific designed loads and boundary conditions. It is worth mentioning that contrary to the large-scale structures, for a micro-scale cellular material, being stretching-dominated is generally an intrinsic property that is independent of boundary conditions or external loadings. 2) Construction materials commonly have a very large modulus of elasticity (and often a very small Poisson's ratio). These assumptions assure that bending or transverse deflections under the given loading conditions are negligible. If the cross sections of the members of the designed structure are proportional to the magnitude of their force given by the force diagram, the resulting system would be a constant-stress structure.^[58] Without losing generality, these assumptions can also be used for designing small-scale strut cellular materials where the boundary and loading conditions are periodic.

This paper investigates the application of geometry-based structural form-finding technique as a topological-based method for designing strut-based cellular and shellular solids. Initially, the paper introduces the geometry-based struc-

tural form-finding technique as an alternative method for designing cellular solids and clarifies the relationship between the geometry, topology, and the flow of force in such system. A methodology is then put forward to devise the unit-cell of strut-based cellular and novel shellular materials by designing the topology and geometry of the force diagram, which is followed by further elaboration on controlling the boundary conditions including the directions and locations of the applied loads and supports. The paper concludes by investigating the effects of various materialization techniques on the linear elastic mechanical performances of a range of designed and devised cellular structures using numerical homogenization and experimental compression tests performed on the samples 3D printed by digital light processing (DLP).

2. Methodology

In this section, after explaining the geometric principles of equilibrium (Section 2.1), the authors introduce the methods of polyhedral graphic statics (PGS) for the design of cellular solids by designing the force distribution's topology (Sections 2.2 and 2.3). Afterward, in Section 2.7, the material properties of a family of cellular materials designed by this method will be evaluated using a multi-scale modeling technique.

2.1. Reciprocal Diagrams, Geometric Principles of Equilibrium, and Related Design Methodology

Following William Rankine's work on the relationship between the equilibrium of polyhedral frames and closed force polyhedra,^[45] Maxwell formulated the geometrical and topological dependencies of a frame and its forces using a pair of reciprocal diagrams.^[44] These form and force diagrams are the basis of the 2D and 3D graphic statics methods that have been evolved as architectural and structural design tools.^[44,46–48]

2.1.1. 2D Reciprocal Diagrams

The form and force diagrams in 2D graphic statics (2DGS) consist of vertices, edges, and polygonal faces. The number of vertices v_i , edges e_i , and faces f_i in the form diagram is equal to the number of faces f_i^\dagger , edges e_i^\dagger , and vertices v_i^\dagger in the force diagram, respectively (Figure 2a). Each edge of the force diagram e_i^\dagger is perpendicular (or parallel depending on the convention) to the corresponding edge e_i in the form diagram. In this article, the edges of the force diagram are perpendicular to their corresponding edges in the form diagram. Moreover, the edges converging to a vertex v_i in the form diagram construct a closed polygonal face f_i^\dagger in the force diagram.^[44] The length of each edge $|e_i^\dagger|$ in the force diagram represents the magnitude of the force in the reciprocal edge e_i of the form diagram (Figure 2a).^[44,45] Each closed polygon in the force diagram shows the static equilibrium of its reciprocal node in the form diagram. Furthermore, if a force diagram consists of closed and convex polygons, then there exists a reciprocal form diagram that is either compression-only

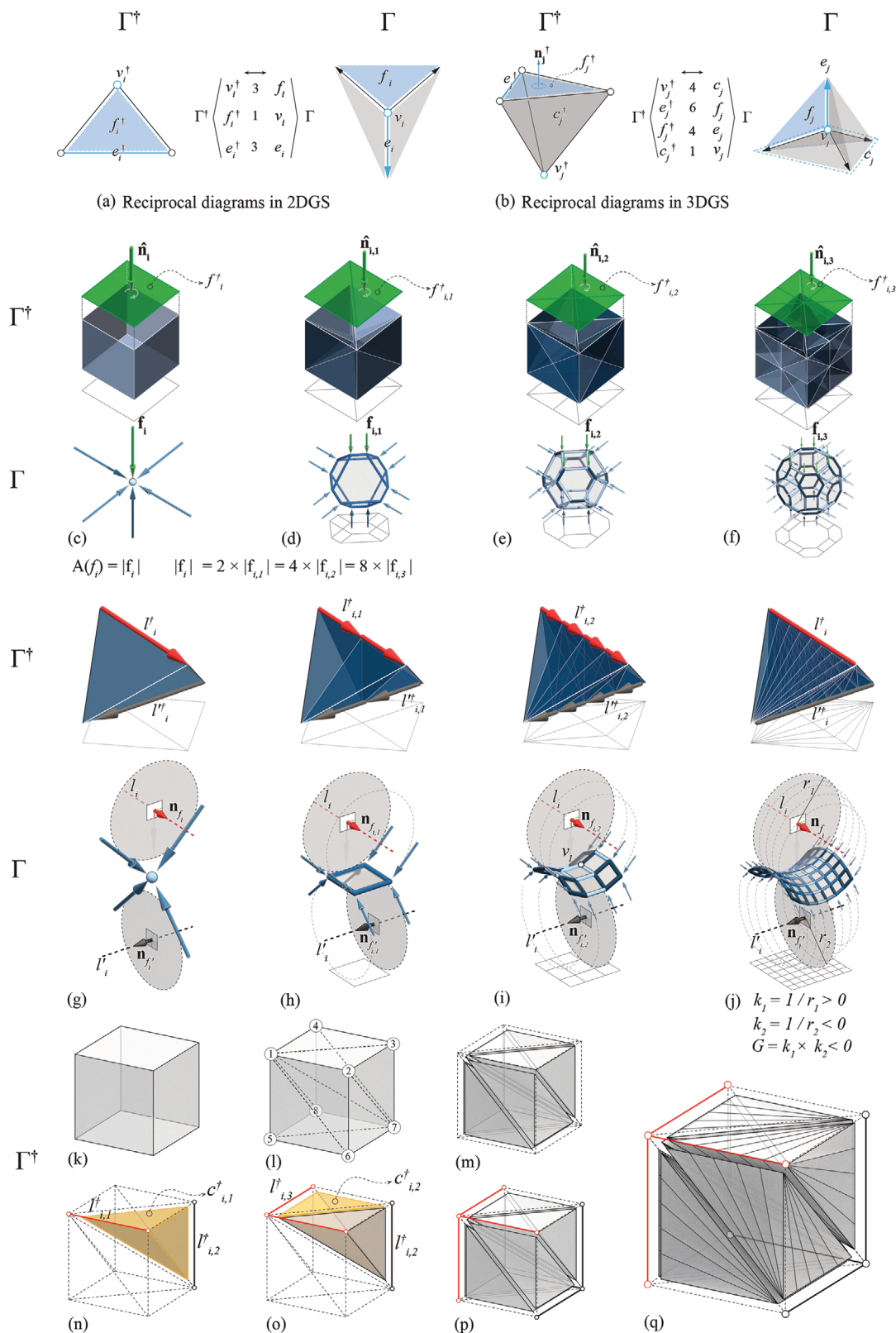


Figure 2. Reciprocal diagrams along with their topological elements in 2D (a) and 3D (b), the process of generating a truss cellular unit cell in PGS via internal subdivision of the force diagram (c–f), the process of approximating an anticlastic surface in PGS (g–j), and the process of identifying the labyrinths and generating the force diagram of a shellular funicular structure (k–q, for the reciprocal form diagrams of these force diagrams, please observe Figure 3b,c).

or tension-only system depending on the direction of the applied loads.^[44]

Let us assume a system of co-planar intersecting bars (e.g., e_i) connected to the vertex v_i , as rope segments in tension (Figure 2a, Γ). To find the magnitude of the force in each segment and showing the equilibrium of the system, a reciprocal force polygon can be constructed by drawing lines perpendicular to the ropes (Figure 2a, Γ^\dagger). If so, the length of each edge vector of the force diagram $|e_i^\dagger|$ represents the magnitude of the force f_{e_i} in the edge e_i of the form diagram (Figure 2a).^[44,45] In this example, a force diagram with 3 vertices, 1 face, and 3 edges, is reciprocal to a form diagram with 3 faces, 1 vertex, and 3 edges, respectively. It should be noted that both form and force diagrams in Maxwell's definition consist of closed polygonal faces that represent the reciprocal relationship and the equilibrium of forces in a self-stressed systems with no externally applied load. In this paper, we use a modified definition in which the external faces of the the form diagram are open. As depicted in Figure 2a, the form diagram includes open external faces. This definition allows the inclusion of the external loads in the form diagram.^[57]

2.1.2. Polyhedral (3D) Reciprocal Diagrams

Aside from the vector-based extensions of graphic statics in 3D,^[48,54,59,60] there is an extension based on reciprocal polyhedral diagrams proposed by Rankine^[45] and Maxwell,^[44] which has been recently clarified and utilized for the design of spatial funicular polyhedral systems.^[57,58,61,62] In this paper, this extension is used as an alternative method for designing cellular solids. As the static equilibrium of a single node in 2D can be geometrically represented by a closed polygon constituting the force diagram (Figure 2a), the static equilibrium of a node in 3D can be represented by a closed force polyhedron with planar faces (Figure 2b).^[63] If the forces $|f_{e_i}|$ applied to a node v_j in space are perpendicular and proportional to the areas of the faces f_j^\dagger of a closed polyhedron, then the summation of the forces will become zero and the node will be in static equilibrium. This property can be proved using Stokes theorem.^[55,64] The node and the applied loads represent the form diagram, while the closed polyhedron represents the force diagram (Figure 2b). Note that in this article, all the elements of the force diagram have been marked with the \dagger sign. Therefore, the magnitude and the distribution of the forces in the members of the form can be visualized by adding thickness to each member of the form diagram proportional to the area of the corresponding face in the force diagram (Figure 2c–f).

The reciprocal polyhedral diagrams are topologically dual and geometrically perpendicular.^[65] Each diagram consists of vertices, edges, faces, and cells. Each edge, vertex, cell, and face in the form diagram (e_j, v_j, c_j, f_j), respectively, corresponding to one and only one face, cell, vertex, and edge ($f_j^\dagger, c_j^\dagger, v_j^\dagger, e_j^\dagger$) of the other diagram (Figure 2b). All faces in both diagrams are planar and all edges e_j are perpendicular to their dual faces f_j^\dagger . Each polyhedron in the system is a proper cell decomposition of space, that is, the cells have disjoint interiors, and every face of one cell is a complete face of another cell.^[57] The direction of the force f_{e_j} in the form diagram follows the direction of

the normal of the corresponding face n_j^\dagger in the force diagram (Figure 2b). Such structural forms carry the forces in the form of axial forces either pure tension or pure compression where the direction of the internal force is perpendicular to the cross section of the element. In addition, the equilibrium of a system that is in pure tension or pure compression can be represented by a force diagram consisting of closed convex polyhedral cells.

2.1.3. Constructing Reciprocal Diagrams

Reciprocal polyhedrons of PGS can be constructed either by using iterative methods^[65] or algebraic methods.^[66,67] Currently, there exist free software packages including PolyFrame,^[68] 3D Graphic Static,^[69] and a computational framework COMPAS,^[70] which are based on iterative methods and are available for designers and researchers. They receive a group of boundary representation surfaces (B-rep) as an input and iteratively construct the dual diagram with edges perpendicular to the faces of the input within a certain predefined tolerance. The algebraic method, on the other hand, constructs these reciprocal polyhedrons in a single step by solving a system of equations around the faces of the dual diagram.^[71,72] Currently, there is no design software available for users based on the algebraic methods. In this paper, we will use PolyFrame^[68] for the construction of the reciprocal diagrams.

2.1.4. Nodal and Global Equilibrium in PGS

The reciprocal polyhedrons are at the core of the methods of polyhedral graphic statics. Since a single closed convex force polyhedron represents the equilibrium of a single node (under pure compression or tension) in 3D (Figure 2c), a subdivision of a closed convex polyhedral cell in a force diagram into multiple closed convex polyhedral cells can then represent the equilibrium of a group of nodes, forming a spatial structural system (Figure 2d).^[65,73] Figure 2c,d shows the subdivision of a cube as a force diagram of a single node in equilibrium, to 12 tetrahedrons as a force diagram of a group of connected nodes in equilibrium. The external faces of the force diagram construct a larger polyhedron encompassing all the smaller polyhedral cells. This external polyhedron corresponds to the global equilibrium of the forces in the dual/reciprocal form diagram and is called global force polyhedron or cell. All internal polyhedral cells in the force diagram represent the equilibrium of the internal forces in each node of the form diagram and are referred to as the nodal force polyhedron. Thus, the global force polyhedron represents the direction and the magnitude of the reaction forces at supports and externally applied loads regardless of the internal topology of the form for a given boundary condition (Figure 2c–f).^[57]

2.2. Subdividing the Force Diagram as a Method of Design

Subdividing the global force polyhedron is a design technique to create various funicular forms for a given boundary condition. In this approach, the external polyhedron, representing the global equilibrium, is subdivided into smaller convex polyhedral cells using various subdivision schemes.^[64,74] Figure 2

shows two examples of a single node and their force polyhedron that can be transformed into topologically different spatial configurations without changing the global equilibrium. Figure 2c shows a single node and its cubic force polyhedron. In each step, the internal and external faces of the global force polyhedron are divided into smaller convex polyhedral cells (Figure 2d–f). Note that the summation of the areas of the faces of the external polyhedron remains constant in all steps. Thus, the global equilibrium does not change for all the configurations. The same procedures are used for the Figure 2g–j where subdividing the global force polyhedron in each step transforms a single node with a tetrahedron force diagram into a discrete surface with an anticlastic curvature (i.e., $G = k_1 \times k_2 < 0$, in which k_1 and k_2 are the surface's principal curvatures).

2.3. Designing Low-Density Cellular Materials by Subdividing A Polyhedral Force Diagram

The methods of PGS can be applied in the design of a force diagram, reciprocal to the geometry of the periodic unit cell of cellular materials. This approach provides a new route for controlling the topology of the cellular architectures. Various subdivisions of a force diagram result in a variety of topologically-different structural forms for a given boundary condition.^[64] In this section, we explain two methods of subdivision to generate strut-based cellular and shell-based cellular (shellular) unit cells using PGS. These techniques result in triply periodic compression-only (or tension-only) cellular materials for a predefined cubic boundary condition (i.e., $\pm x$, $\pm y$, and $\pm z$).

2.4. Designing Strut-Based Cellular Funicular Unit Cells

The design of a unit cell of a triply periodic cellular material starts with a global force polyhedron that can be aggregated in three directions in a 3D space (Figure 1a–d). A simple cube with 6 faces can be chosen as the global force polyhedron of a unit cell with 6 applied and reaction forces (Figure 2c). Different types of subdivisions of a force diagram allow to develop a wide range of strut-based cellular unit cells. For instance in Figure 2c–f, the external face f_i^\dagger in the force diagram Γ^\dagger is reciprocal to the external load \mathbf{f}_i in the form diagram Γ , and the area of the face $A_{f_i^\dagger}$ equals to the magnitude of the force $|\mathbf{f}_i|$. In Figure 2d, the face f_i^\dagger is divided into two faces where the force $f_{i,1}^\dagger$, for instance, corresponds to an external load $\mathbf{f}_{i,1}$ ($|\mathbf{f}_i| = 2|\mathbf{f}_{i,1}| = A_{f_i^\dagger}$). It should be mentioned that with each subdivision of the external faces, the internal space is also subdivided by connecting the external faces to the centroid of the initial cell. This procedure assures that in every step the internal cells stay closed and convex. Figure 2d,e,f shows recursive subdivision processes, which result in 12, 24, and 48 tetrahedrons. The resulting form diagram is a pin-jointed network representing the force-flow in a tension-only or compression-only system. This system can be materialized by adding thickness to the edges of the network to construct a strut-based cellular architecture, as shown in Figure 1a,b. Adding thickness to the faces of the form results in a polyhedron-based cellular solid as shown in Figure 1e,f. Both results can be aggregated

in three directions to create a cellular material. Under compression, the structural performance of the low-density strut-based cellular materials designed using this approach can also rely on the buckling performance of the struts. Increasing the number of subdivisions while keeping the volume constant, results in shorter edges with a lower magnitude of internal force, reducing the slenderness ratio of the struts (after materialization), and increasing the maximum buckling capacity.^[56,75] Using particular design techniques, the members can become extremely small, translating the cellular form to a shell-based cellular architecture.

2.5. Designing Shell-Based Cellular Funicular (Shellular)

Shellulars are ultra-low density materials composed of a single, continuous, smooth-curved shell (Figure 1i–l).^[3] Increasing the number of subdivisions in the force diagram results in a form diagram with shorter edges (Figure 2g–j). The subdivision process can be designed such that the lengths of the edges of the form diagram become extremely small (Figure 2j). These short members may approximate a discrete spatial shell. There are particular methods of subdivisions (e.g, anticlastic subdivision, Section 2.5.1) in PGS resulting in a polyhedral surface geometry with synclastic or anticlastic properties.^[74,76]

2.5.1. Anticlastic Geometries in PGS

In a discrete anticlastic surface as a pin-jointed network, at each node (called anticlastic node), two edges are curved upwards (hanging) and two are curved downward (standing), corresponding to an anticlastic curvature at that node. Similarly, in Figure 2g, a tetrahedron as a global force polyhedron is reciprocal to a node with four applied loads, two upward and two downward (form diagram). In fact, subdividing this tetrahedron in multiple steps gives global force polyhedrons for discrete anticlastic surfaces as shown in Figure 2g–j. Note that the subdivision transforms the anticlastic node to a discrete anticlastic surface. In this example, the force diagram has two skew edges, l_i^\dagger , red, and $l_i^{\dagger\prime}$, black, that can be subdivided recursively to make smaller tetrahedrons. In this process, the skew edges l_i^\dagger and $l_i^{\dagger\prime}$ are divided into an equal number of segments such that each segment of the former will make a tetrahedron with its associated segment in the latter (Figure 2h).^[76] The form diagram as a result of this subdivision is a polyhedral surface with an anticlastic curvature.

Further subdivision of those edges results in a smoother surface as a form diagram (Figure 2i,j). This particular type of subdivision is named anticlastic subdivision. In this type of subdivision, the nodal polyhedral cells are tetrahedrons. This results in a reciprocal, valency-four vertices (e.g., v_1) in the form diagram (Figure 2i). Vertex v_1 is connected to two hanging and two standing edges, establishing a negative Gaussian curvature. The resulting anticlastic surface of Figure 2g–j is only subjected to the applied loads in its boundaries. As shown in Figure 2j, the curvature axes in an anticlastic surface, l_i and l_i' , are parallel to the subdivision axes in the reciprocal force diagram l_i^\dagger and $l_i^{\dagger\prime}$. These axes are referred as labyrinths in the design of shellular materials.

2.5.2. The Role of Labyrinths in Designing and Controlling the Geometry of Shellular Materials

An anticlastic surface geometry of Figure 2j divides the 3D space into two subspaces (top and bottom) separated by the shell geometry. These subspaces can also be identified by their curvature axes l_i and l'_i . In fact, these axes may represent the connectivity graph of these subspaces in complex shellular geometries that are often referred as labyrinths.^[77,78] In this paper, these labyrinths have been marked with red and black colors (e.g., **Figure 3**). The labyrinths in anticlastic geometries are two intertwined graphs whose edges are always in a skew position with each other. The two labyrinths interpenetrate each other while the anticlastic surface is in between (Figure 2j). The geometry of the surface changes when the angle of these labyrinths changes.^[77] Interestingly, the labyrinths in the form and force diagrams of PGS are related as follows (Figure 2g–j): a) the labyrinth l_i of the form is parallel to the l'_i of the force diagram; and b) the labyrinth l_i is the axis of curvature in the form diagram while its parallel labyrinth in the force diagram is the subdivision's axis. The topology of an anticlastic surface can be described by its labyrinths.^[77] In fact, a force diagram can be subdivided following the geometry and topology of prescribed labyrinths; a reciprocal compression-only or tension-only anticlastic shell can be constructed, for a designed loading condition, using the methods of PGS.

2.5.3. The Labyrinths' Design Principles

In order to properly design the labyrinths' sets in PGS, certain geometrical and topological requirements should be satisfied. These requirements define the labyrinths' design principles and are as follows:

- 1) Tetrahedralization: Each pair of labyrinths' edges in the force diagram should form a tetrahedron in between, corresponding to a node with an anticlastic curvature in the form diagram. Applying an anticlastic subdivision to the tetrahedron transforms it to multiple tetrahedrons, converting the node to a polyhedral surface with anticlastic curvature in the form diagram (Figure 2g–j). This polyhedral surface only includes valency-4, anticlastic nodes. Therefore, in order to design a discrete shellular architecture, one needs to decompose the force polyhedron (global force polyhedron) into proper non-overlapping tetrahedra (e.g., Figure 3b).
- 2) Skew labyrinths: Each force diagram corresponding to a shellular architecture contains two sets of labyrinths. After subdividing the force diagram to a group of tetrahedra, each tetrahedron only includes one labyrinth edge from each set in a skew position to the other. For instance, in Figure 3b, $l'_{i,1}$ from the first set (red) and $l_{i,1}$ from the second set (black) are in a skew position to each other.
- 3) Labyrinths' continuity: In a subdivided force diagram, each labyrinth edge in a tetrahedron can only be connected to the labyrinth' edges from the same set in the neighboring tetrahedral cell (Figure 3b–e). This assures that the surface in between the labyrinths' sets in the form diagram divides the space into two sub-spaces sharing the surface in between.

2.5.4. Translating a Strut-Based Cellular to a Shellular Funicular Unit Cell

Section 2.4 described the process of designing a strut-based cellular funicular unit cell in PGS. For designing a shellular funicular unit cell, one can design a cellular version and translate it to the shellular counterpart in PGS (Figure 2k–q). This process starts with a cuboid force diagram which is possible to aggregate in three directions (Figure 2k). In the simplest version, each cube as a force diagram corresponds to one node with six external forces as the form diagram (Figure 3a). The process of translating this cube into the force diagram of a shellular funicular unit cell includes three steps: tetrahedralization, identifying the labyrinth's edges, and applying the anticlastic subdivision.

- 1) Tetrahedralization: To result in a unit cell with an anticlastic geometry that only includes valency-four vertices (Section 2.5.1), one needs to decompose the cube (force diagram) into non-overlapping tetrahedra or tetrahedralize the cube.^[79] There are infinite possibilities to tetrahedralize a cube, but the simpler solutions are the ones that start from the vertices and the edges of the cube.^[80] For instance, in this example (Figure 2l), by connecting the vertex v_1 to the vertices v_3 , v_6 , v_7 , and v_8 and connecting the vertex v_7 to the vertices v_2 , v_4 , and v_5 , one can decompose a cube into six tetrahedrons (Figure 2m). The dual structure that is constructed from this force diagram is a network of six connected vertices with 12 external forces in equilibrium (Figure 3b). It is worth mentioning that different tetrahedralization results in different force diagrams, form diagrams, labyrinths' sets, and subsequently, different geometry of shellular funicular unit cells.^[81]
- 2) Identifying the labyrinths' edges: From each of these tetrahedrons, one can select two skew edges in order to create two intertwined labyrinths' graphs that are separated from each other. After starting from a tetrahedron $c_{i,1}$ and highlighting its skew labyrinths' edges $l'_{i,1}$ and $l_{i,2}$ (Figure 2n), the labyrinths' edges of the neighbor cell $c_{i,2}$ will be highlighted based on its shared labyrinth's edge $l'_{i,1}$ with cell $c_{i,1}$ (Figure 2o). This process continues until all the cells are parsed and their labyrinth edges are determined (Figure 2p). In this process, each labyrinth's graph remains continuous and does not touch its pair graph (Section 2.5.3). Since one can choose three different pairs of labyrinth edges in each tetrahedron, this method may result in three geometrically different labyrinths' graphs. Further information in this regard has been explained in Sections S2.1 and S2.2, Supporting Information.
- 3) Applying the anticlastic subdivision: After identifying the labyrinths in the tetrahedralized force diagram, one may apply the anticlastic subdivision (Section 2.5.1) between each pair of labyrinths' edges in each tetrahedron to result in a smoother version of the form diagram (Figures 2q and 3c). Increasing the the level of anticlastic subdivision in each tetrahedron results in a smoother form diagram with higher resolution (Section 2.5.1).

This process results in the force diagram corresponding to a patch of Schwarz P surface (Figure 3d,e). In fact, each well-known minimal surface includes two sets of labyrinths

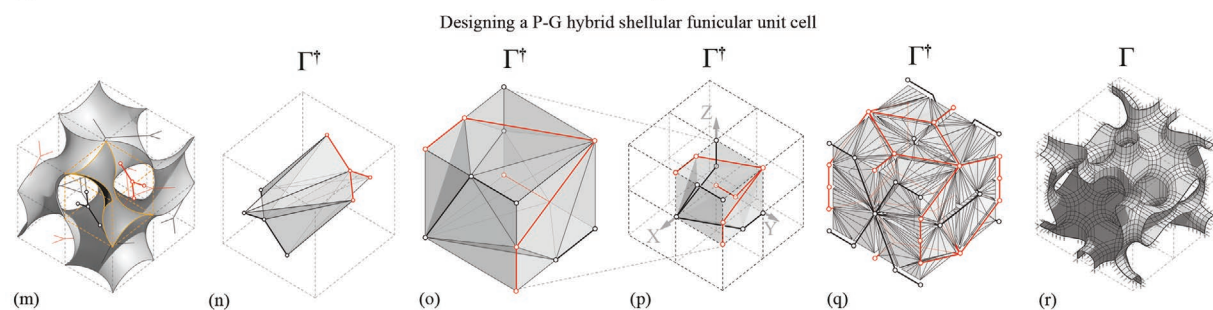
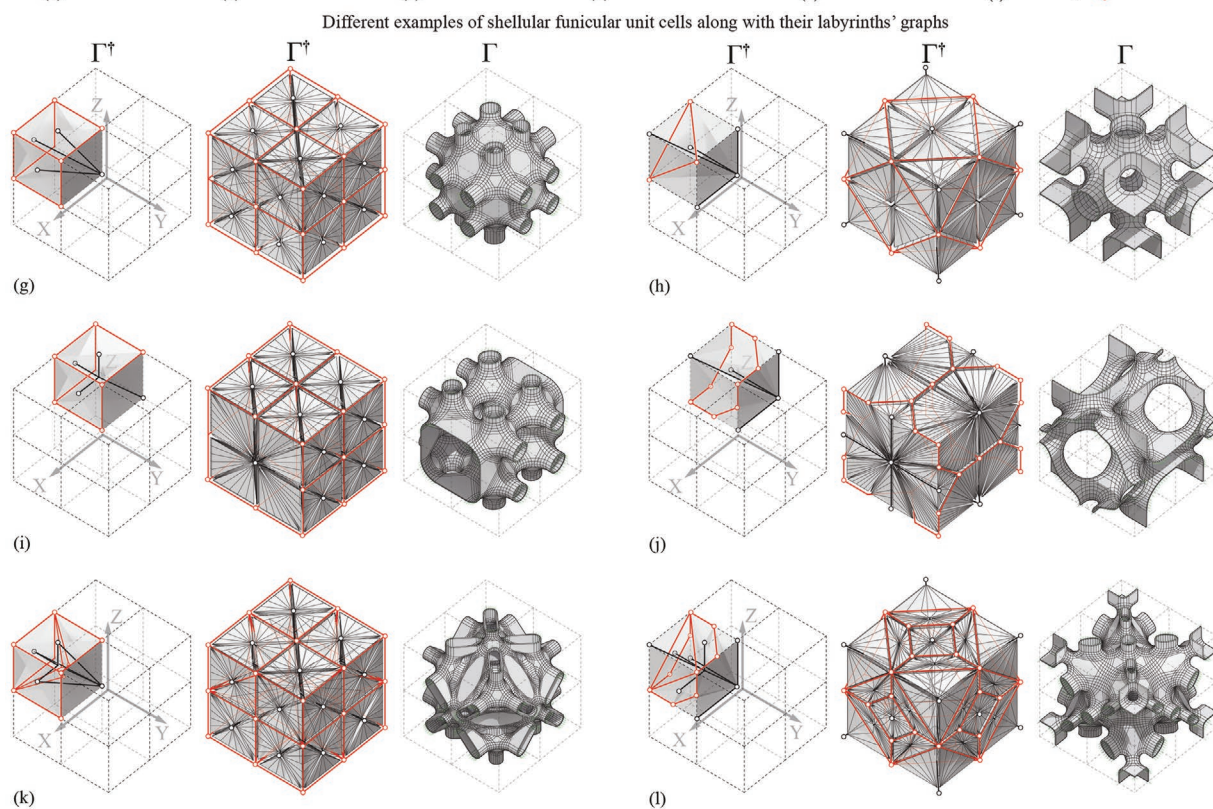
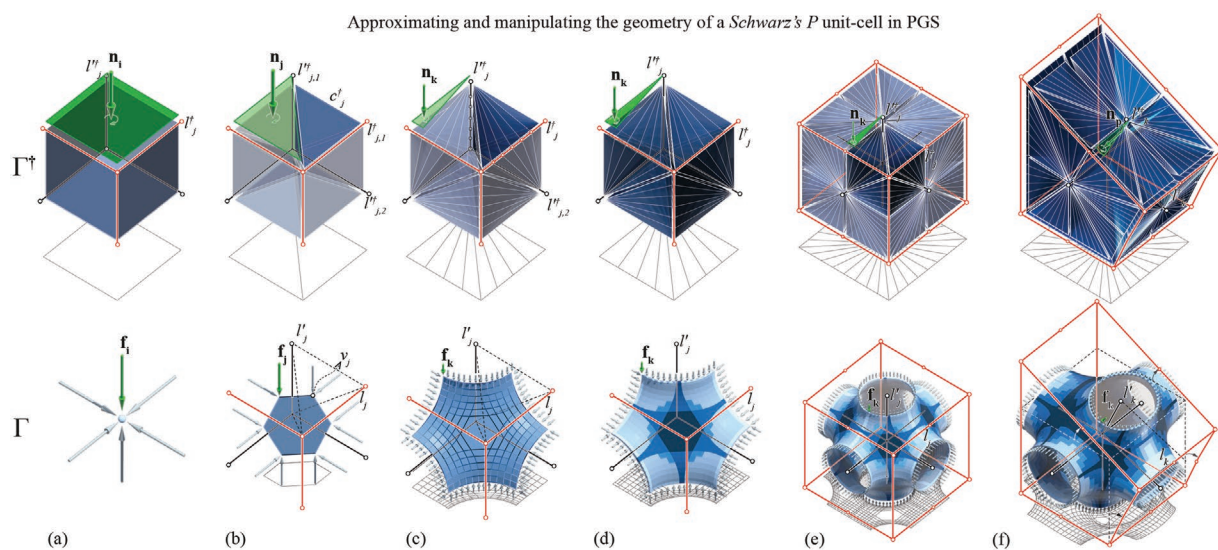


Figure 3. a–f) The process of approximating a compression-only unit cell of the Schwarz's P surface, g) approximation of Schwarz's W unit cell, h) a Schwarz P-Gyroid hybrid unit cell (Section S2, Supporting Information), and i–n) different examples of P-W hybrid unit cells designed in PGS.

that can be used to approximate its geometry. By changing the level of the anticlastic subdivision, one can control the resolution of the well-known minimal surface, from a strut-based cellular to a shell-based cellular (shellular) unit cell (Section 2.5.5). Figure 3g–l depicts different examples of shellular funicular unit cells that have been designed with this method. In each example, the tetrahedralization of the 1/8 section of a force diagram along with the force and the form diagram of a shellular funicular unit cell have been shown. The form-finding flowchart of this process, along with the visual representation of the workflow have been depicted in Section S2.3, Supporting Information.

2.5.5. Approximating Well-Known Minimal Surfaces Using PGS

This section explains the main steps for approximating the geometry of a Schwarz P unit cell as a well-known minimal surface in PGS (Figure 3a–f). In order to approximate the force diagram of a well-known minimal surface in PGS, one needs to superimpose its labyrinths to a cube, tetrahedralize the cube based on the labyrinths, and finally add the anticlastic subdivision.

- 1) As mentioned before (Sections 2.4 and 2.5.4), the global force polyhedron corresponding to a repeatable unit cell in three directions is a cube.
- 2) According to the literature, Schwarz P's labyrinths consist of two sets of 3D graphs, one as a cubic wire-frame with 12 edges and the other as six intersecting edges perpendicular to each other (Figure 3e).^[82]
- 3) As the labyrinths in the form diagram play the role of the subdivision axes in the force diagram, to design the force diagram, one needs to superimpose the labyrinths' graphs on the cubic force diagram.
- 4) Owing to the reflection symmetries in the geometry of the Schwarz P unit cell, the design process can be simplified by designing 1/8 section of the unit cell, comprising two labyrinths' sets with three edges perpendicular to each other (e.g., $l_{i,1}^{\uparrow}$), and in skew positions to their peer (e.g., $l_{i,1}^{\downarrow}$) in the second set (Figure 3b).
- 5) In the force diagram, each labyrinth's edge $l_{i,1}^{\uparrow}$ from the first labyrinths' set is in a skew position with two labyrinth edges, $l_{i,1}^{\downarrow}$ and $l_{i,2}^{\downarrow}$, in the second set (Figure 3b). Forming a tetrahedron cell between each pair of skew labyrinth edges subdivides the global force polyhedron to six tetrahedrons, each corresponding to a node (e.g., v_j) connected to two edges and two external forces in the form diagram (Figure 3b) (the tetrahedralization of a force diagram based on the existing labyrinth graphs have been explicitly explained in Section S3, Supporting Information).
- 6) As explained in Section 2.5.1, applying the anticlastic subdivision to each tetrahedron (similar to Figure 2g–j) subdivides the current force diagram to 216 tetrahedrons, corresponding to a semi-smooth polyhedral surface with anticlastic curvature, as a form diagram (Figure 3c).
- 7) Adding thickness to the faces of the form diagram proportional to the area of the average of the corresponding faces in the force diagram (Figure 3d) materializes the network to

a shellular funicular geometry. This geometry approximates 1/8 section of the Schwarz P cell.

8. Due to the reflection symmetry of the Schwarz P, mirroring the geometry of the force diagram about the x , y , and z coordinate planes, results in a reciprocal form diagram, approximating a Schwarz P unit cell as a compression-only anticlastic shell (Figure 3e).
9. Capitalizing the explicit correlation between the geometry of the labyrinths and the reciprocal diagrams, manipulating the former's geometry results in changing the geometry of the latter. Figure 3f shows deformation of the Schwarz P unit cell by manipulating the labyrinths' geometries toward a new unit cell that is designed for a different boundary condition.

Repeating these steps for new sets of labyrinths enables designers to approximate other well-known minimal surfaces' unit cell in PGS such as Schwarz W (Section S3.2, Supporting Information). The angle between each pair of labyrinths, the length of each edge in a labyrinth set, the distance between a labyrinth's edge and its pair, and the valence of each vertex of a labyrinth's graph (the number of edges connected to the vertex) are the main parameters affecting the geometry of the labyrinths' graphs and subsequently the resulting shellular architecture.

2.5.6. Designing a P-G Hybrid Shellular Funicular Unit Cell

This section explains the design process of a hybrid shellular funicular unit cell in PGS. This model results from the combination of the labyrinths' sets of the Gyroid's surface (mapped to a cube) and the symmetry of the Schwarz's P surface (Figure 3m–r).

- 1) Identifying the Gyroid's patch's labyrinths: Since this method intends to apply the symmetry of the Schwarz's P surface, one needs to start from 1/8 of the Gyroid's surface (Figure 3m), and apply the reflection symmetry. Therefore, the design process starts with 1/8 section of the Gyroid's surface (Gyroid's patch) comprised of two sets of labyrinths. Each labyrinth's set includes three edges and the angle between each two edges is 120 degrees.
- 2) Mapping the labyrinths to a cube: As mentioned in Section 2.4, a global force polyhedron that can be aggregated in three main directions is a cube. To translate this cube to the force diagram of a shellular funicular unit cell, one needs to make sure the cube is a proper decomposition of non-overlapping tetrahedra. Generating tetrahedrons between labyrinths sets of Gyroid's patch does not decompose the whole cube to tetrahedrons (Figure 3n). Hence, one needs to map the labyrinths' graphs to the cube in a way that all the labyrinth's design principles are satisfied (Figure 3o). This process is explained explicitly in the Section S2, Supporting Information. After mapping the labyrinths, a tetrahedron is generated between each pair of labyrinth edges. Applying an anticlastic subdivision between each pair of labyrinth's edge in each tetrahedrons results in a force diagram corresponding to the form diagram of the Gyroid's patch which is mapped to a cube.

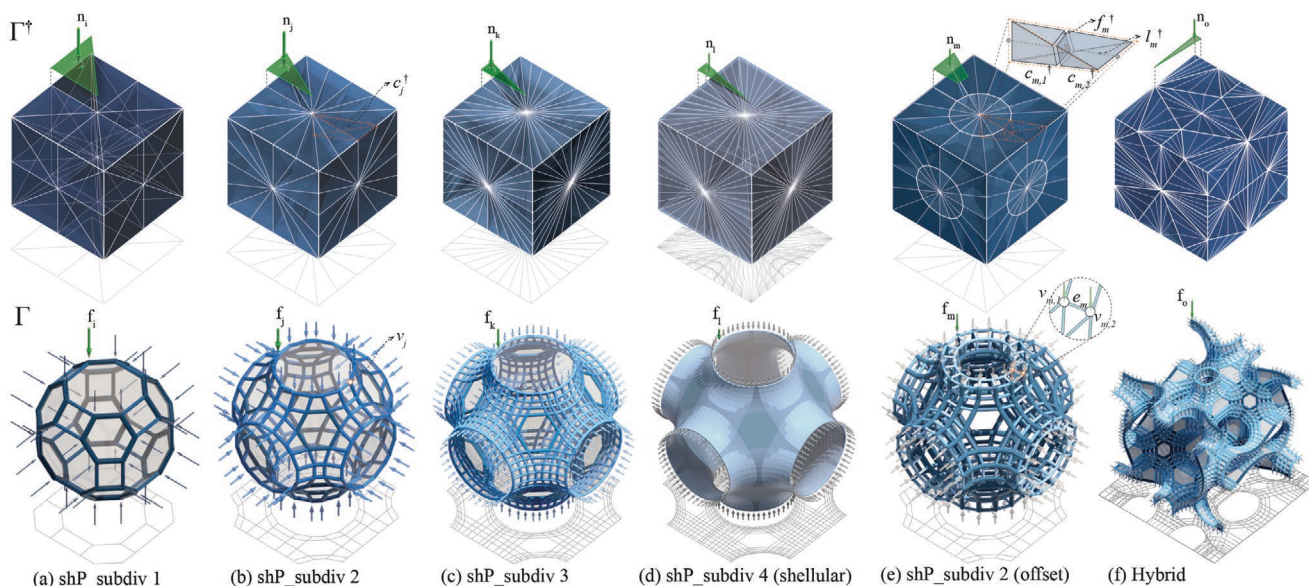


Figure 4. Form and force diagrams of a group of specimens that are designed using PGS and are mechanically analyzed in Section 2.7.

3) Applying the Schwarz's P symmetry: Gyroid's unit cells has neither planar nor straight lines symmetries.^[83] Therefore, applying a reflection symmetry (similar to the Schwarz's P surface) changes the geometry of the unit cell. For applying a cubic symmetry, after considering three symmetrical planes in three directions (pl_{xy} , pl_{yz} , and pl_{zx}), one can reflect the force diagram in three directions to result in the new unit cell's force diagram (Figure 3p,q). The reciprocal form diagram of this force diagram is a P-G hybrid unit cell (Figure 3r).

2.6. A Family of Cellular Materials Designed in PGS

Figure 4 depicts the form and force diagrams of a group of specimens that are designed using the PGS method. It shows a range of reciprocal diagrams that are designed based on the Schwarz P labyrinths' geometries. Based on the process explained in Section 2.5.5, by increasing the number of subdivisions in the force diagram, one can design a group of structures with different resolutions, from strut-based cellular (Figure 4a) to shellular funicular structure (Figure 4d). Increasing the number of subdivisions leads to decreasing the area of faces in the force diagram resulting in a form with less force in each member. Figure 4e shows the force and form diagrams of a double layer version of the shP-subdiv2 (Figure 4b). Subdividing the cell c_j^\dagger in shP-subdiv2 to two cells $c_{m,1}^\dagger$ and $c_{m,2}^\dagger$ using the face f_m^\dagger (Figure 4e) converts each vertex v_j in shP-subdiv2 to two vertex $v_{m,1}$ and $v_{m,2}$ connecting with an edge e_m in shP-offset. It is worth mentioning that the angle of the face f_m^\dagger in the force diagram determines the angle off the edge e_m in the form diagram (Figure 4e). Aligning the face f_m^\dagger perpendicular to the axis l_m^\dagger in the force diagram assures us that the edges connecting the two layers (e.g., e_m) are somehow perpendicular to each layer in the form diagram. The last specimen (Figure 4f) depicts the force and form diagrams of

a hybrid model which is designed based on combining the labyrinth sets' geometry of the Schwarz P and gyroid surfaces (Section S2, Supporting Information).

2.7. Multi-Scale Modeling for Evaluating Material Properties of Cellular Architectures

2.7.1. CAD Modeling

To materialize the designed truss-like cellular architectures, joint locations together with the diameters of the struts connecting each two joints are saved in a text format and later read by a SolidWorks macro to create all the struts and merge them, producing a unit cell of the corresponding cellular material. As it will be discussed in the results and discussion section, in addition to cylindrical struts, double cone struts (Figure 7a) with $D/d = 4$ are also considered to further tune the cells' mechanical properties. Considering that connected struts at one joint generally do not lie on a plane and their diameters can vary, struts are modeled with spherical end caps to prevent undesirable holes, cavities, and abnormal joint topologies (Figure S9, Supporting Information). This not only resembles the physical attachment of struts (as compared to the simplified frictionless joints with no moment resistance assumed in previous sections), but also facilitates discretization of the cellular materials in the numerical simulations.

The designed shellular architectures are also realized by adding thickness to either sides of the middle surface created by patching the network of the struts' center lines. Smooth P and G shellulars based on the trigonometric level set equations:

$$\begin{aligned} P : \cos x + \cos y + \cos z &= 0 \\ G : \cos x \sin y + \cos y \sin z + \cos z \sin x &= 0 \end{aligned} \quad (1)$$

are modeled in SolidWorks by first creating a subset of the surface using boundary curves and several points or curves that

satisfy the corresponding equation and exploiting their inherent symmetries to construct the mid-surfaces of the unit cell. To ensure the periodicity of the RVEs, merged $2 \times 2 \times 2$ pattern of the unit cell's mid-surface is then thickened and subsequently cut into the cubic RVE.

2.7.2. Numerical Homogenization

Detailed modeling and numerical analysis of cellular materials and structures comprising many unit cells are arguably complex and computationally expensive. Numerical homogenization provides a tool to replace a heterogeneous cellular architecture by a homogeneous solid medium with matching effective properties, thus significantly reducing the complexity and the computational cost of a detailed numerical analysis. Homogenization techniques have recently been used to evaluate mechanical,^[84] thermal,^[18] and electromechanical^[85] properties of architected cellular solids. Replacing a periodic heterogeneous cellular architecture with an equivalent homogeneous base material requires the existence of several unit cells throughout the cellular materials to ensure the periodicity of stress and strain fields along the neighboring cells.^[86–88] Under this assumption, it is possible to acquire the effective mechanical properties of cellular architectures using the standard mechanics homogenization technique applied to a representative volume element (RVE) under periodic boundary conditions (PBC). While loading on the RVE can be either in the stress or strain form, herein six independent strain loading cases (i.e., $\bar{\epsilon}^j = [\bar{\epsilon}_{xx}^j, \bar{\epsilon}_{yy}^j, \bar{\epsilon}_{zz}^j, \bar{\epsilon}_{xy}^j, \bar{\epsilon}_{yz}^j, \bar{\epsilon}_{xz}^j]$, where the superscripts denote the loading case number and the only non-zero strains are $\bar{\epsilon}_{xx}^1 = \bar{\epsilon}_{yy}^2 = \bar{\epsilon}_{zz}^3 = 2\bar{\epsilon}_{xy}^4 = 2\bar{\epsilon}_{yz}^5 = 2\bar{\epsilon}_{xz}^6 = 1$ are applied pointwise to the corresponding node pairs belonging to the periodic boundary surface mesh (Figure S10, Supporting Information) through:

$$\left\{ \begin{matrix} u_x \\ u_y \\ u_z \end{matrix} \right\}_{\Gamma^+} - \left\{ \begin{matrix} u_x \\ u_y \\ u_z \end{matrix} \right\}_{\Gamma^-} = L_i \begin{bmatrix} \bar{\epsilon}_{ix}^j \\ \bar{\epsilon}_{iy}^j \\ \bar{\epsilon}_{iz}^j \end{bmatrix} \quad i = x, y, z \quad j = 1, 2, \dots, 6 \quad (2)$$

in which, superscripts represent the loading case number, u_x , u_y and u_z are the components of the nodal displacement vector; Γ^+ and Γ^- identify the positive and negative RVE faces that contain the boundary nodes (Figure S12, Supporting Information); and L_i represents the dimension of the cuboid RVE along x , y , or z direction. Additionally, zero displacement is imposed on an arbitrarily selected node to avoid rigid body motion. Under each loading case, volumetric averages of the resultant stresses over the elements constituting the RVE (i.e., $\sigma^j = [\sigma_{xx}^j, \sigma_{yy}^j, \sigma_{zz}^j, \sigma_{xy}^j, \sigma_{yz}^j, \sigma_{xz}^j]$) are used to construct rows of the 6×6 linear elastic stiffness matrix C of the equivalent homogenized material using:

$$C(j, \dots) = \frac{1}{V_{RVE}} \int \sigma^j dV_{RVE} \quad j = 1, 2, \dots, 6 \quad (3)$$

Effective Young's and shear moduli and Poisson's ratios (\bar{E} , \bar{G} , and $\bar{\nu}$, respectively) are then calculated from the C matrix. To focus solely on the role of cell architecture and exclude the

contribution of the underlying linear elastic solid material, the two moduli are normalized by the Young's modulus of the base solid material (E_s). More details about the standard mechanics homogenization can be found in ref. [86].

Numerical finite element analysis in this article is carried out using Ansys simulation software. Quadratic mesh elements, with at least two elements through the thickness of struts/shells, are used to ensure the accuracy of the computational results and to reduce the number of trials for the mesh sensitivity analyses. Additionally, deformations are assumed small and buckling or nonlinearities are not considered.

3. Results and Discussion

In this section, effective mechanical properties of the materialized periodic architectures, designed based on the method introduced in Sections 2.5.5 and 2.5.6, are investigated to evaluate their linear elastic performances and to discuss the potentials of this novel design methodology for engineering architected cellular solids. Additionally, cell relative densities $\bar{\rho}$ (defined as V_s/V_{RVE} where V_s and V_{RVE} denote the volume of the solid material in the unit cell and the volume of the RVE, respectively) are confined to 0.01 to 0.05 to focus the discussion on lightweight architected cellular materials.

3.1. Architected Cellular Materials Mimicking Schwarz P

Having developed a family of truss-like cellular and shellular architectures resembling Schwarz P in Section 2.5.5, their normalized effective Young's and shear moduli (\bar{E}/E_s and \bar{G}/E_s), and Poisson's ratios ($\bar{\nu}$) are examined in Figure 5. Considering the inherent cubic rotational symmetries of these mechanically orthotropic cellular materials, only \bar{E}_x , \bar{G}_{xy} , and $\bar{\nu}_{xy}$ are reported. As shown, mechanical properties of the designed shellular based on the subdivision 4, match with those of the level-set based P shellular. It is also expected that increasing the subdivision number shall decrease the differences between the two, since the subdivision scheme here acts as structural form refinement and controls the smoothness of the shell. Although the same trend can be observed for the elastic moduli of the truss-like cellular counterparts and the cellular materials get stiffer by increasing the subdivision number from 1 to 3, their effective mechanical properties cannot reach to those of the P shellular as the selected subdivision scheme cannot cover the whole surface (no strut can pass through the center of the empty central hexagon in Figures S13 and S14, Supporting Information). Furthermore, struts are always parallel to one of the coordinate planes using this subdivision scheme, hence, even with several subdivisions each small polygonal part of the cell will never behave as a 2D isotropic material and unlike P shellular, the local mechanical response of the mesh-like network is anisotropic throughout the cell. It is possible to reduce the in-plane mechanical anisotropy of a polygon by introducing diagonal members, referred to as bracings. Similarly, bracings can also be added to the discussed empty hexagons. It is worth mentioning that these bracings are not part of the original idealized design methodology (which yields the idealized cells that

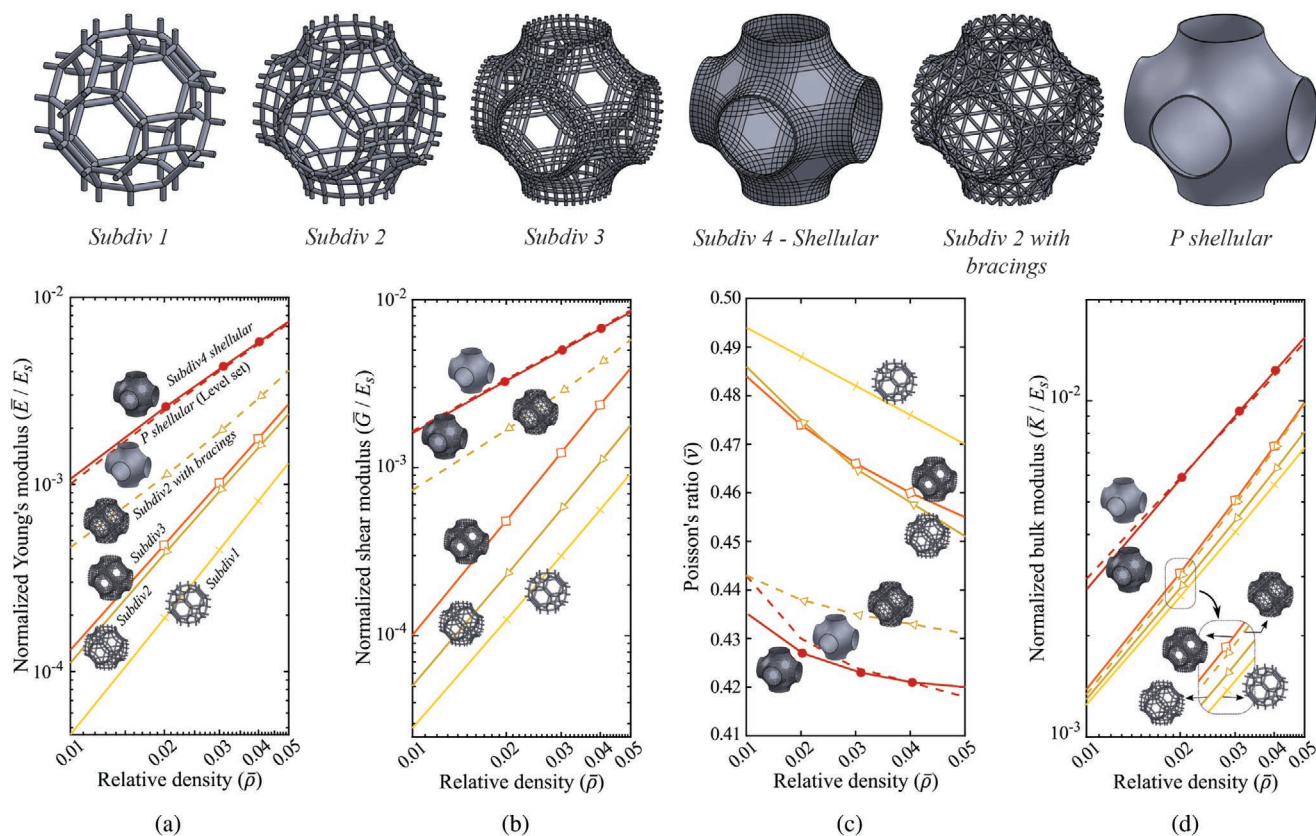


Figure 5. Effective mechanical properties of a family of cellular materials resembling Schwarz P. a) Young's modulus, b) shear modulus, c) Poisson's ratio, and d) bulk modulus. Poisson's ratio of the base solid material $\nu_s = 0.3$.

consist of two-force rigid members connected to each other by frictionless joints, making up mechanisms with no state of self-stress rather than cellular materials), and are being introduced to showcase how reducing the number of inextensional mechanisms and increasing the number of states of self-stress of the original designed ideal truss can stiffen the cellular material counterpart and shift its properties toward those of the P shellular (sample study is provided in Section S11, Supporting Information).

Considering that introducing the bracings invalidates some of the original design considerations including the equal stresses in the struts that is used to determine the diameter ratios of the constitutive struts, bracings are added while all struts and bracings have equal diameters. As presented in Figure 5a–c, compared to the original Subdiv2, the new cellular material (i.e., Subdiv2 with bracings) is considerably stiffer and its effective E , G , and ν are significantly closer to the P shellular.

While Young's and shear moduli of the three designed strut-based materials (Subdiv1, 2, and 3) are generally orders of magnitude smaller than those of the P shellular, their bulk moduli K are relatively closer to the P shellular (Figure 5d), which originates from the assumed triaxial loading as their design boundary conditions. In this regard, as discussed before, the idealized truss architectures are all mechanisms (hence the small \bar{E} and \bar{G}); however, under a periodic triaxial loading, they are statically determinate, resulting in high \bar{K} values. Comparing P shellular with the truss-like architectures without

bracings at $\bar{\rho} = 0.01$, \bar{E} of the shellular cell is more than ten times greater, however its \bar{K} is only about two times greater. This good performance of the three subdivision cells under triaxial loading can be correlated to their Poisson's ratios that are close to 0.5. Using the relation between K , E , and ν of the orthotropic materials with cubic rotational symmetries that is given by $\bar{K} = \bar{E} / [3(1 - 2\bar{\nu})]$, a Poisson's ratio close to 0.5 creates a very small denominator which significantly amplifies the right-hand-side division and consequently results in a high bulk modulus even when Young's modulus is small. Von Mises stress distributions over the materialized RVE of Subdiv1, 2, and 3 under periodic triaxial strains are presented in Section S12, Supporting Information, to show how stresses in a cellular material deviate from the idealized design in which struts have equal stresses when the RVE is under a triaxial loading. The observed stress distributions on different cells at different relative densities are rationally justified based on their average strut slenderness ratios.

An alternative approach in designing the struts of the cellular architectures is to ignore the stress uniformity assumption and adopt equal diameters for all struts. Effective mechanical properties of the Subdiv1, 2, and 3 with equal strut diameters reveal negligible alterations in $\bar{\nu}$ when compared with their original subdivision cells. \bar{E} and \bar{K} of the Subdiv1 variant with equal strut diameters both show about 3% decrease, while its \bar{G} exhibits approximately 9% increase with respect to Subdiv1 designed based on equal strut stresses under triaxial load. While

\bar{K} of the Subdiv2 with equal strut diameters shows negligible drop, the change in its \bar{E} and \bar{G} are more pronounced, being -7% and 11% , respectively. \bar{K} of the Subdiv3 variant with equal strut diameters also shows negligible drop, while on average its \bar{E} and \bar{G} display 9% decrease and 13% increase, respectively. The variation in the effective mechanical properties caused by changing the strut diameters demonstrates the possibility of tuning the architecture for a specific mechanical requirement, while the topology is kept constant and only struts diameters are altered. Considering that a simple 1D beam model can be used to efficiently predict the mechanical behavior of slender struts, effective properties of the Subdiv1, 2, and 3, obtained by modeling the struts with

1D beam elements, are compared with those presented in Figure 5 in Section S13, Supporting Information. Additionally, the effect of the base material's Poisson's ratio on the homogenized linear elastic properties of the strut-based cellular materials are investigated in Section S14, Supporting Information.

3.2. Architected Hybrid Shellular

To showcase the potentials of the introduced design methodology for developing novel cellular architectures, effective linear elastic mechanical properties of a hybrid shellular are investigated. As discussed in Section 2.5.6, the P-G hybrid cell is designed to have the inherent reflection symmetries of the

P shellular about the coordinate planes (i.e., $x = 0$, $y = 0$, and $z = 0$ planes), while one-eighth of the cell is developed based on a deformed subset of the gyroid using shellular funicular structures' method (SHS). Inspiration for developing the hybrid architecture comes from the contrast in mechanical performances of P and G shellulars, for which when $0.01 \leq \bar{\rho} \leq 0.05$, the former is highly anisotropic and exhibits greater effective shear modulus and Poisson's ratio (\bar{G}_{ii} and $\bar{\nu}_{ij}$, respectively, when $i, j = x, y, z$ and $i \neq j$) while the latter exhibits near isotropy and greater Young's modulus (\bar{E}_{ii} when $i = x, y, z$). Mechanical anisotropy of the discussed shellulars is quantified using Zenner ratio $\alpha = \bar{E} / [2\bar{G} (1 + \bar{\nu})]$.

Figure 6 compares \bar{E} , \bar{G} , and $\bar{\nu}$ of the three shellulars. As presented, compared to the P shellular, the P-G hybrid shellular shows a significantly lower level of anisotropy (as its Zenner ratio is closer to 1), while outperforming its stiffness. This, however, comes at the price of having smaller \bar{G} . On the other hand, the effective mechanical properties of the P-G hybrid shellular are evidently outperformed by the G shellular, which is believed to be partially caused by the imposed form deformation on the gyroid's subset during the design phase, which in turn alters stress distribution and the in-plane dominance of shell properties, and potentially magnifies out-of-plane deformations. As demonstrated by this example, the proposed methodology in this article can be used for designing novel cellular architectures with new mechanical properties.

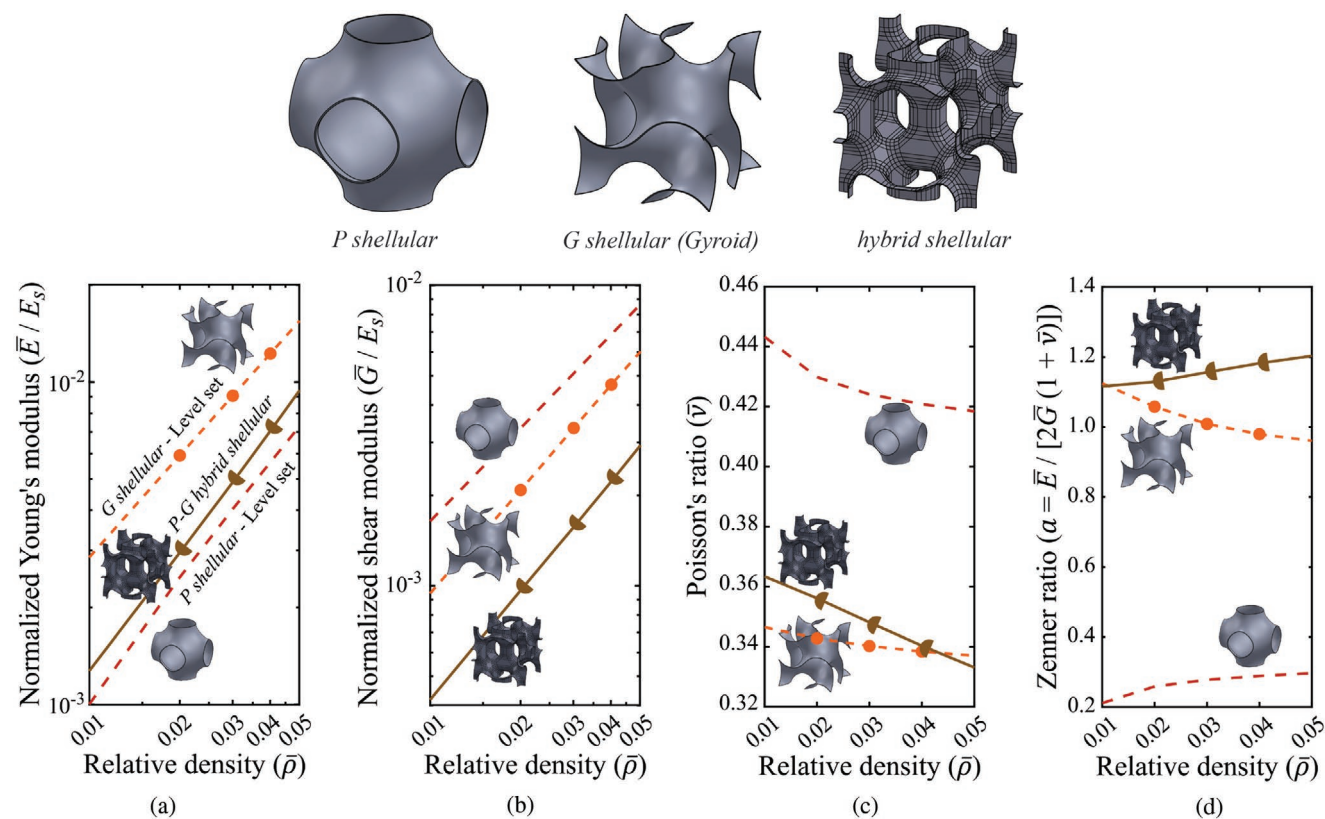


Figure 6. Comparing effective mechanical properties of an architected hybrid shellular material with P and G shellulars: a) Young's modulus, b) shear modulus, c) Poisson's ratio, and d) Zenner anisotropic ratio. Poisson's ratio of the base solid material ν_s is assumed 0.3.

3.3. Double Layer Truss-Like Cells

In previous parts of the discussion section, subdivision terminology is used as a tool to refine the topology of the architecture; however, as it generally refers to subdividing the force and form diagrams, it can also account for changing other architectural characteristics of a cell. As an example, while Subdiv2 cell has interconnected struts only in one layer, using the presented procedure in Section 2.6, a novel architecture resembling Subdiv2 with two layers of interconnected struts (denoted as Offset cell in Figure 7) are designed to showcase another attractive feature of the proposed cellular material design methodology. Effective mechanical properties of these two variants of subdivision 2 (respectively named Subdiv2 and offset) are compared in Figure 7b. As presented in this figure, \bar{E} , \bar{G} , and \bar{K} of offset cellular material are less than those of Subdiv2, as opposed to $\bar{\nu}$. The slightly smaller \bar{E} of offset cell is justified by the alignments of the struts connecting its two layers, some of which bear little to no load while it experiences a uniaxial load. In addition, while strut lengths on the two layers of offset cell are approximately the same as those of Subdiv2, with the increased number of struts the average slenderness ratio $\bar{\lambda}$ is significantly increased (for $\bar{\rho}$ equal to 0.01 and 0.05, the calculated $\bar{\lambda}$ are, respectively, 9.7 and 4.2 for offset cell, as compared to 5.9 and 2.5 for Subdiv2 cell), reducing the effects of joints and making the struts behave more similarly to the two-force link assumption used during the design procedure. As a result of this increase in the average slenderness ratio, under triaxial loading offset cell shows more uniform stress distribution

compared to Subdiv2 as presented in Figure S14d, Supporting Information. The smaller joints and slenderer beams, resulted from having higher numbers of struts and joint valencies, amplify the mechanism nature of this new architecture, and result in a significant reduction in \bar{G} and a slight increase in $\bar{\nu}$ (which is already extremely close to 0.5). Furthermore, the close \bar{K} of Subdiv2 and its offset variant can be justified by entering the aforementioned slight increase in $\bar{\nu}$ and the decrease in \bar{E} in their correlation with bulk modulus as $\bar{K} = \bar{E} / [3(1-2\bar{\nu})]$.

As discussed earlier, the designed cellular architectures in this section owe their large \bar{K} to the triaxial loading condition during the architectural design process, under which their idealized trusses are statically determinate; while under the uniaxial or shear loads, the unstable idealized trusses act as mechanisms, leading to their small \bar{G} . To further increase the \bar{K}/\bar{G} ratio of Subdiv2 and offset cellular architectures, cylindrical struts are replaced by double cones (Figure 7a) that significantly decrease their \bar{G} by making the joints smaller and reducing their resistance against bending moment. It is worth noting that while different criteria (such as equal stress, equal diameter or equal slenderness ratio) can be implemented to materialize a cell, for cells with either of cylindrical or double cone members, diameter ratios between different struts are considered to be based on the equal stress criterion. Additionally, ratio of the middle to the end diameters of the double cone members D/d (Figure 7a) is considered to be 4.

The inspiration for using double cone struts comes from pentamodal metamaterials, theoretically developed by Milton

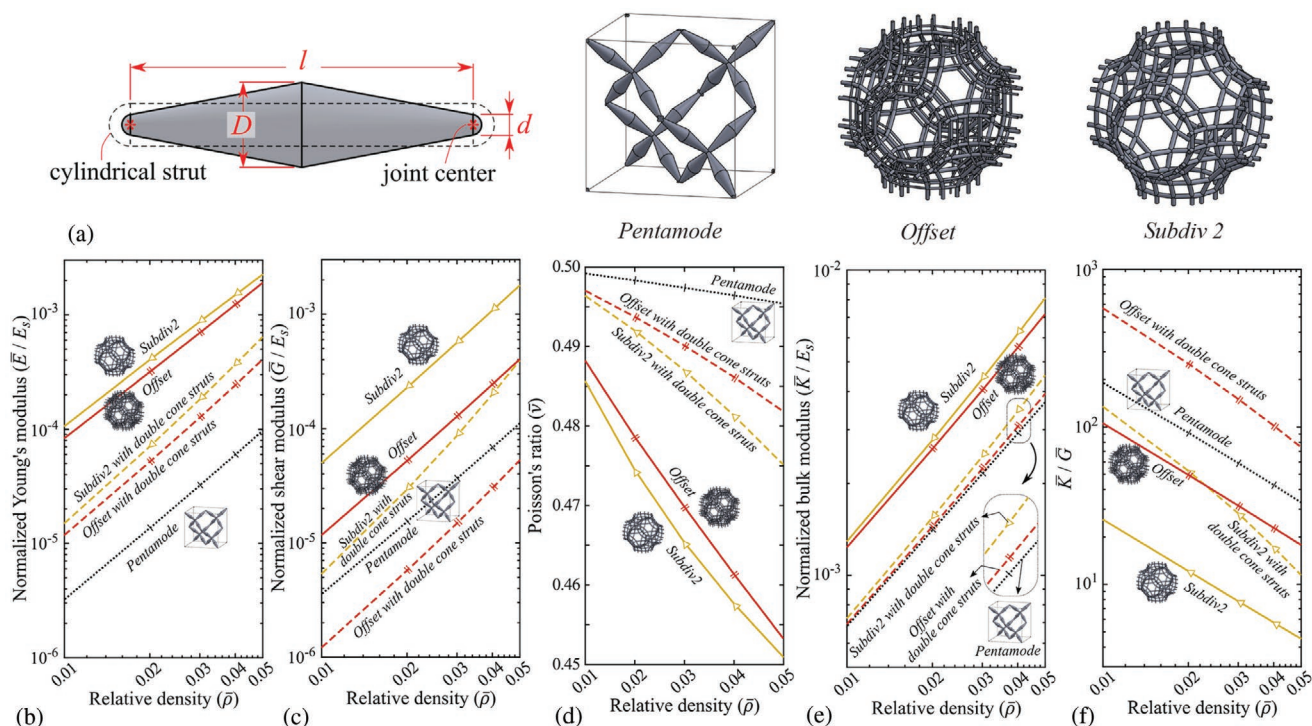


Figure 7. Cylindrical and double cone strut dimensions (a) and comparing effective mechanical properties of Subdiv2, Subdiv2 with double cone struts, offset with double cone struts, and pentamode cells: b) Young's modulus, c) shear modulus, d) Poisson's ratio, e) bulk modulus, and f) \bar{K}/\bar{G} ratio. D/d of the double cone struts is 4.

and Cherkaev,^[89] which are difficult to compress but easy to flow. This fluid like behavior (i.e., $G \approx 0$ and $\nu \approx 0.5$) is achieved by avoiding the coupling of compression and shear waves using extremely large \bar{K}/\bar{G} .^[89–91] Mathematically speaking, five of the six diagonal elements of the diagonalized 6×6 elasticity tensor of these metamaterials are either zero or really close to zero, hence the word “Penta”. Promising potential applications such as elastic cloaking devices,^[92] shear wave band gap systems,^[93] and seismic isolation devices^[94] are proposed for pentamode metamaterials, although their generally small \bar{E} might hinder their practical utilization.

Effective mechanical properties of a pentamode architecture, originally proposed in,^[89] are compared with those of Subdiv2 and offset cells, together with their double cone strut variants in Figure 7. As presented, while using double cone struts is shown to increase $\bar{\nu}$, the three elastic moduli \bar{E} , \bar{G} , and \bar{K} are decreased since the double cone struts exhibit less resistance to tensile or bending deformations as compared to cylindrical struts with the same volume and length. Additionally, \bar{K}/\bar{G} ratios of the cells with double cone struts are significantly increased as intended (Figure 7f). Comparing the pentamode with the double-cone-strut offset cellular architecture, the latter shows significant improvement in Young’s modulus and \bar{K}/\bar{G} ratio (more than three and more two times, respectively) while its shear modulus is considerably smaller (more than two times). Accordingly, the double-cone-strut offset cell paves the way toward practical applications of metafluid cellular metamaterials by presenting a stiffer alternative with \bar{K}/\bar{G} greater than 1000 while its relative density is only slightly below 0.01 (at which it is 3.6 times stiffer, while its \bar{K}/\bar{G} ratio is about 570, as compared to pentamode with $\bar{K}/\bar{G} \approx 190$).

4. Additive Manufacturing and Experimentation on 3D Printed Cellular Materials

Manufacturability of the designed cellular architectures are demonstrated here using digital light processing (DLP) 3D printing, in which a sample is printed layer by layer by exposing a photopolymer resin to UV light.^[95] Figure 8a–e showcases some of the 3D printed parts using this method. While some imperfections, such as rough surface finish, small distortions, holes/bubbles, and partial strut connectivity are present in 3D printed samples, exploring possible methods to reduce these imperfections are beyond the scope of this article. Comparing the elastic properties of the as-built 3D printed samples, determined by conducting experimental tests and the numerical simulation predictions, confirms that the imperfections have minimum impact on the elastic performance of funicular materials. A single setup with the same settings is used for DLP 3D printing and post processing of all samples. It is also worth mentioning that no internal support has been used for DLP 3D printing since the selected funicular materials comprise short and thick struts, and the interconnected struts of funicular materials do not allow removal of 3D printing support materials.

To investigate the validity of numerically determined homogenized Young’s moduli as compared to the experimental data, architected cellular samples shall contain plenty of unit cells along different directions to minimize the effects of the non-periodic boundary cells and keep the periodicity assumption in homogenization valid. Manufacturing a complex 3D cellular architecture, containing multiple cells and small enough for testing, generally demands a highly accurate 3D printing technique such as digital light processing. Considering the cell

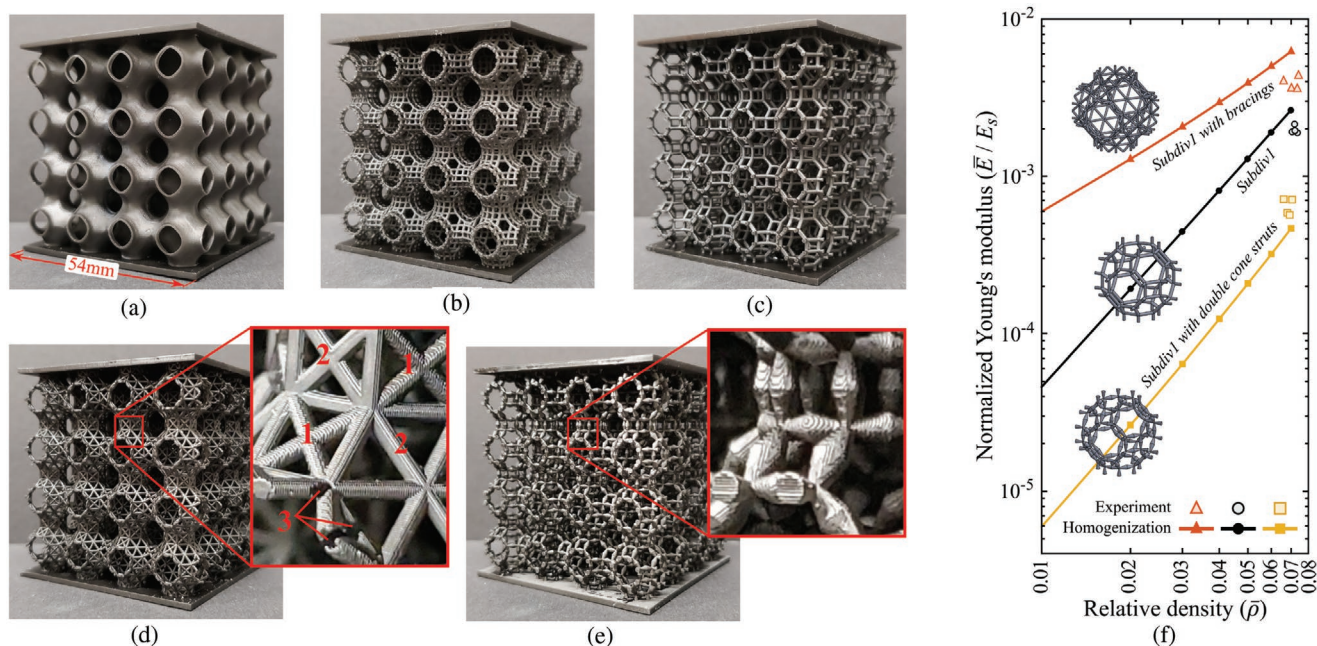


Figure 8. 3D printed cellular samples: a) P Shellular, b) Subdiv 2, c) Subdiv 1, d) Subdiv1 with bracing, and e) Subdiv1 with double cone struts. f) Comparing the numerically determined normalized effective Young’s modulus \bar{E}/E_s with the experimental results for Subdiv1, Subdiv1 with bracings, and Subdiv1 with double cone struts cellular architectures.

features and limitations imposed by printing size and accuracy, variants of Subdiv1 (the cellular architecture with the thickest struts among the discussed cells in previous sections), that is, Subdiv1, Subdiv1 with bracings, and Subdiv1 with double cone struts are selected to minimize the effects of printing deficiencies. Subdiv1 cell contains the minimum number of struts; therefore, for the same relative density, it possesses the thickest cell members. Subdiv1 with double cone struts is made by replacing the cylindrical struts of Subdiv1 with double cones (Figure 7a) with $D/d = 4$. To design the Subdiv1 with bracings cell, bracings are added to Subdiv1 and equal diameter is used for all struts and bracings.

Samples for experimental testing contain $4 \times 4 \times 4$ unit cells between two plates at the bottom and top sides (Figure 8a–e), with the as-designed cell relative density of 0.05. B9 Core 550 DLP machine (B9Creations) is used to 3D print samples out of brittle B9R-2-Black Resin (B9Creations). The two plates are added to prevent the early failure of the small struts as a result of their direct contact with the compression platens. After 3D printing, the four samples for each architecture type are washed in isopropyl alcohol for 20 min using B9clean unit, to make sure the excessive uncured resin is completely removed from the surface of the members. Afterward, using the high-intensity UV post-curing B9 model cure unit, each sample is cured separately under water for 15 min, consisting of two 5 min and two 150 s curing, each followed by turning the sample to ensure uniform post-curing. Details about the cellular models, 3D printing, and post-processing are listed in Table 1.

Mechanical compression tests are performed using a 20 kN dual column ADMET universal testing machine, under a displacement rate of 5 mm min^{-1} . Engineering stress (force divided by the initial $54 \times 54 \text{ mm}$ cross section) and engineering strain (displacement divided by the initial 54 mm height of the cellular section of the samples) are used to calculate effective Young's moduli of the 3D printed cellular materials. As presented in Section S14, Supporting Information, the obtained stress–strain curves exhibit an initial toe region in which the slope gradually increases; an artifact caused by skewed top and bottom plates and/or a take-up of loose seating of the specimen. Since this toe region does not represent a material property, effective Young's moduli are estimated by the maximum slope of the stress–strain curves right after the toe region.

Table 1. Cellular models, 3D printing, and post-processing details.

Cellular sample's overall size	$54 \times 54 \times 56.7 \text{ mm}$ (containing $4 \times 4 \times 4$ unit cells and two 1.35 mm thick plates)
3D printer	B9 Core 550 DLP printer (by B9Creations)
Material	B9R-2-Black Resin (by B9Creations)
Layer height	50 microns
Cleaning unit	B9clean (by B9Creation)
Cleaning material	IPA
Cleaning time	20 min
Curing unit	B9 model cure (by B9 Creation)
Curing method/ time	Under water at room temperature for 15 min ($2 \times 5 \text{ min} + 2 \times 150 \text{ s}$ with turning the sample between steps)

After compression tests, the remaining connected struts are removed from the top and bottom plates and as-built densities of the cellular materials are calculated by subtracting the weight of the plates from the initial weights of the samples, and dividing the resultant by the volume of the sample's cellular portion. Dividing the obtained apparent density with the density of the base solid material (measured as 1.13 g cm^{-3}) yields the relative density of each cellular sample. Although the 3D printed samples are based on CAD models of cellular solids with $\bar{\rho} = 0.05$, the as-built relative densities are close to 0.07 and the extra material is not uniformly distributed over the cell members, which is the result of noticeable printing defects on small struts and features, especially on those further away from being perpendicular to the printing bed. Furthermore, while corners are sharp inside the CAD model, they are inevitably rounded on the 3D printed parts, adding the weight to the sample and reducing the stress concentrations that affects the overall mechanical properties compared to the numerical simulation conducted on the as-designed samples.

To measure the Young's modulus of the 3D printed base solid material, dogbone samples are also prepared under the similar setup as the 3D printed cellular parts. As presented in Section S15, Supporting Information, tensile test coupons with different 3D printing alignments: flat, perpendicular, and inclined

to the build plate of the 3D printer, are produced to examine the effects of printing direction on the material's stiffness. During the preliminary tests, it is observed that the measured Young's modulus of the base solid material exhibits some degrees of dependency with the time span between the curing process and the tensile test. While this can be attributed to different factors such as room temperature and/or humidity, further exposure to UV light or a probable chemical reaction with air, probing into this phenomenon is out of the scope of this article; hence, to keep the experiments consistent, all post processed dogbone and cellular samples are stored in the same location for about a week before conducting the mechanical tests. Tensile tests are performed using a universal testing machine (20 kN dual column ADMET), under the displacement rate of 5 mm min^{-1} . The obtained Young's moduli, defined as the slope of the linear curve fitting through the first 0.001 strain, show no significant dependency with the printing direction and are averaged at $1421 \pm 116 \text{ MPa}$ as the Young's modulus of the base material (E_s).

Figure 8f provides the comparison between the numerically obtained normalized effective Young's moduli \bar{E}/E_s with those from the compression tests. Similar to the case of Subdiv2 and its variants discussed in the previous sections, the homogenization results show that using double cone struts significantly decreases \bar{E} of Subdiv1, whereas introducing bracings reduces the DOFs of the underlying mechanism of Subdiv1, making it considerably stiffer. Although the experimental results in Figure 8f confirm this trend, having only four cells (instead of many, as considered in numerical homogenization) along the three orthogonal directions, additional top and bottom plates, and the defects in the geometries of joints, corners, and struts of the 3D printed architectures logically lead to the deviation of the experimentally determined Young's moduli from the numerical homogenization predictions. Moreover, with the

default 3D printing layer thickness of 50 micron for all samples, decreasing the feature size or strut diameter amplifies the aforementioned deviation as a result of limited in-plane precision of the 3D printer. Accordingly, as presented in Figure 8d, Subdiv1 with bracing which not only has thinner struts than Subdiv1 but also the additional bracing members have worse overhung angles compared to the struts of Subdiv1, shows noticeable printing deficiencies in its members, such as stair-like, non-cylindrical, and partially connected struts (respectively highlighted inside the image with 1, 2, and 3). These printing defects lead to noticeable deviation of experimental data and numerical predictions for the elastic moduli of Subdiv1 with bracing, compared to Subdiv1 and Subdiv1 with double cone struts. A higher resolution additive manufacturing technique, such as two-photon lithography (TPL),^[95] can facilitate more accurate realization of the as-designed low-density architected cellular materials in order to attain closer properties of the as-built samples and the numerical predictions.

5. Concluding Remarks

This article introduces a novel systematic approach for topological design of lightweight architected strut- or shell-based cellular materials using 3D graphic statics. The proposed methodology provides a synergistic correlation between the internal force distribution, geometry, and the external boundary conditions, paving the way toward rational designs of periodic or non-periodic funicular truss architectures. It is found that successive distribution of the internal forces through numerous struts with progressively shorter lengths can transform a bending-dominated strut-based funicular structure to a shellular architecture with significantly improved mechanical properties. Furthermore, the relations between the underlying labyrinths of the form and force diagrams of the shellular structures are used to devise unprecedented shell-based architectures, either by generating new labyrinths or by deforming and/or combining existing ones. While one can choose any arbitrary criterion to control shape and cross-section of the struts in a funicular architecture, here cylindrical struts based on constant stress or diameter as well as double-cone struts are adopted to materialize a selected set of designed periodic cells. Additionally, introducing bracing members to the sub-architecture of a funicular cell is discussed as an alternative intermediate step in transforming truss cells to shellulars. To investigate the mechanical properties of the materialized cellular architectures, standard mechanics homogenization is applied on their unit cell under a periodic boundary condition and their effective Young's and shear moduli and Poisson's ratio (\bar{E} , \bar{G} , $\bar{\nu}$, respectively) are numerically determined. The wide range of attained effective mechanical properties of the selected cellular structures with relative densities lower than 0.05 demonstrates the robustness of the proposed design methodology and materialization schemes in developing application-specific lightweight cellular materials spanning from soft and bending-dominated to stiff and stretching-dominated architected mechanical metamaterials for structural applications. The developed methodology can also serve as a framework for developing novel shellulars with hybrid topologies that present tuned mechanical properties with potential applications in engineering

tissue scaffolds, or for designing pentamode-inspired materials with exotic metafluidic behavior for elasto-mechanical unfeability cloaking. While the paper focuses on designing cell architectures, effect of choosing different base solid materials on the linear elastic mechanical performance of the designed cellular architecture is also examined through varying the Poisson's ratio of the isotropic constituent solid material (ν_s) between 0.01 and 0.49. Comparing the homogenized properties of strut-based cellular architectures with relative densities below 0.05 shows a small dependency of the effective moduli on ν_s , rendering their effective linear elastic properties valid for a wide range of underlying solid materials. On the other hand, mechanical properties of shellulars exhibit higher dependency on ν_s as a result of higher material connectivity. Ultimately, the numerically obtained mechanical properties are compared with those extracted from the compression tests on cellular samples, 3D printed by DLP technique. The observed agreement between the two further endorses the presented design and materialization techniques and highlights the manufacturability of the funicular strut-based cellular materials by additive manufacturing, shedding light on the real-life multifunctional applications of efficiently designed funicular cellular and shellular materials.

Supporting Information

Supporting Information is available from the Wiley Online Library or from the author.

Acknowledgements

M. Akbari and A. Mirabolghasemi contributed equally to this work. This research was funded by the National Science Foundation CAREER Award (NSF CAREER-1944691 CMMI) and the National Science Foundation Future Eco Manufacturing Research Grant (NSF, FMRG-CMMI 2037097) to M. Akbarzadeh, and by Natural Sciences and Engineering Research Council of Canada (RGPIN-2016-0471) and Canada Research Chairs program in Multifunctional Metamaterials to A.A. The authors acknowledge the contribution of Hossein Mofatteh, AM³L laboratory at McGill University, in the 3D printing process.

Conflict of Interest

The authors declare no conflict of interest.

Data Availability Statement

The data that support the findings of this study are available from the corresponding author upon reasonable request.

Keywords

3D graphic statics, cellular materials, effective mechanical properties, mechanical metamaterials, reciprocal polyhedral diagrams, shellular, topological modeling

Received: September 25, 2021

Revised: November 29, 2021

Published online:

- [1] T. A. Schaedler, W. B. Carter, *Annu. Rev. Mater. Res.* **2016**, *46*, 187.
- [2] M. Munsch, in *Laser Additive Manufacturing*, Elsevier, New York **2017**, pp. 399–420.
- [3] S. C. Han, J. W. Lee, K. Kang, *Adv. Mater.* **2015**, *27*, 5506.
- [4] L. J. Gibson, M. F. Ashby, *Cellular Solids: Structure and Properties*, Cambridge University Press, Cambridge **1999**.
- [5] G. Savio, S. Rosso, R. Meneghello, G. Concheri, *App. Bionics Biomech.* **2018**, *2018*, 1654782.
- [6] M. C. Fernandes, J. Aizenberg, J. C. Weaver, K. Bertoldi, *Nat. Mater.* **2021**, *20*, 237.
- [7] L. R. Meza, S. Das, J. R. Greer, *Science* **2014**, *345*, 1322.
- [8] R. Jardin, F. Fernandes, A. Pereira, R. A. de Sousa, *Mater. Des.* **2015**, *68*, 121.
- [9] M. F. Ashby, *Philos. Trans. R. Soc., A* **2006**, *364*, 15.
- [10] T. DebRoy, H. Wei, J. Zuback, T. Mukherjee, J. Elmer, J. Milewski, A. M. Beese, A. d. Wilson-Heid, A. De, W. Zhang, *Prog. Mater. Sci.* **2018**, *92*, 112.
- [11] H. Wu, W. Fahy, S. Kim, H. Kim, N. Zhao, L. Pilato, A. Kafi, S. Bateman, J. Koo, *Prog. Mater. Sci.* **2020**, *111*, 100638.
- [12] J. Bloomenthal, K. Ferguson, in *Proc. of the 22nd Annual Conf. on Computer Graphics and Interactive Techniques*, ACM, New York **1995**, pp. 309–316.
- [13] A. L. Mackay, *Physica* **1985**, *131*, 300.
- [14] Z. Gan, M. D. Turner, M. Gu, *Sci. Adv.* **2016**, *2*, 5e1600084.
- [15] S. Hyde, Z. Blum, T. Landh, S. Lidin, B. Ninham, S. Andersson, K. Larsson, *The Language of Shape: The Role of Xurvature in Condensed Matter: Physics, Chemistry and Biology*, Elsevier, Amsterdam **1996**.
- [16] S. C. Han, K. Kang, *Mater. Today* **2019**, *31*, 31.
- [17] S. C. Han, J. W. Lee, K. Kang, *Adv. Mater.* **2015**, *27*, 5506.
- [18] A. Mirabolghasemi, A. Akbarzadeh, D. Rodrigue, D. Therriault, *Acta Mater.* **2019**, *174*, 61.
- [19] C. Bonatti, D. Mohr, *Acta Mater.* **2019**, *164*, 301.
- [20] S. C. Han, J. M. Choi, G. Liu, K. Kang, *Sci. Rep.* **2017**, *7*, 13405.
- [21] H. Niknam, A. H. Akbarzadeh, *Mater. Design* **2020**, *196*, 109129.
- [22] S. Rajagopalan, R. A. Robb, *Med. Image Anal.* **2006**, *10*, 693.
- [23] J. Shi, H. Mofatteh, A. Mirabolghasemi, G. Desharnais, A. Akbarzadeh, *Adv. Mater.* **2021**, *33*, 2102423.
- [24] J. R. Greer, V. S. Deshpande, *MRS Bull.* **2019**, *44*, 750.
- [25] Granta Design Ltd, CES selector, Computer software, 2005, <http://www.grantadesign.com/products/ces/>.
- [26] T. A. Schaedler, A. J. Jacobsen, A. Torrents, A. E. Sorensen, J. Lian, J. R. Greer, L. Valdevit, W. B. Carter, *Science* **2011**, *334*, 962.
- [27] V. Deshpande, M. Ashby, N. Fleck, *Acta Mater.* **2001**, *49*, 1035.
- [28] J. Hong, T. Li, H. Zheng, Y. Ma, *Chin. J. Aeronaut.* **2020**, *33*, 1260.
- [29] M. G. Lee, J. W. Lee, S. C. Han, K. Kang, *Acta Mater.* **2016**, *103*, 595.
- [30] M. Rippmann, P. Block, *Proc. Inst. Civil Eng.-Const. Mat.* **2013**, *166*, 378.
- [31] J. Wolff, *Clin. Orthop. Relat. Res.* **2010**, *468*, 1056.
- [32] G. Poleni, *Memorie Istoriche della gran cupola del tempio vaticano*, Number 33 in Padova: Nella Stamperia del Seminario **1748**.
- [33] R. Hooke, *A Description of Helioscopes, and Some Other Instruments*, John Martyn, London **1675**.
- [34] D. Piker, Kangaroo physics, 2013, <http://www.food4rhino.com/project/kangaroo>.
- [35] A. Kilian, Cadenary tool v.1 [computer software], <http://www.designexplorer.net/projectpages/cadenary.html> (accessed: March 1, 2009).
- [36] K. Linkwitz, H. J. Schek, *Ing.-Arc.* **1971**, *40*, 145.
- [37] M. R. Barnes, *Int. J. Space Struct.* **1999**, *14*, 89.
- [38] S. Adriaenssens, P. Block, D. Veenendaal, C. Williams, *Shell Structures for Architecture, Form Finding and Optimization*, Routledge, Oxfordshire, England **2014**.
- [39] E. Morsch, *Reinforced Concrete, Theory and Application*, Verlag Konrad Wittwer, Stuttgart **1912**.
- [40] J. Mata-Falcón, D. T. Tran, W. Kaufmann, J. Navrátil, in *Computational Modelling of Concrete Structures: Proceedings of the Conference on Computational Modelling of Concrete and Concrete Structures (EURO-C 2018)*, CRC Press Balkema, Leiden, The Netherlands **2018**, pp. 641–650.
- [41] M. P. Bendsøe, O. Sigmund, *Arch. Appl. Mech.* **1999**, *69*, 635.
- [42] Y. Yang, C. D. Moen, J. K. Guest, *J. Eng. Mech.* **2014**, *141*, 04014106.
- [43] P. Varignon, *Nouvelle mecanique ou statique*, Claude Jombert, Paris **1725**.
- [44] J. C. Maxwell, *London, Edinburgh Dublin Philos. Mag. J. Sci.* **1864**, *27*, 294.
- [45] W. M. Rankine, *London, Edinburgh Dublin Philos. Mag. J. Sci.* **1864**, *27*, 92.
- [46] W. S. Wolfe, *Graphical Analysis: A Text Book on Graphic Statics*, McGraw-Hill book Company, New York **1921**.
- [47] C. Culmann, *Wildbäche, vorgenommen in den Jahren 1858, 1859, 1860 und 1863* **1864**.
- [48] L. Cremona, *Graphical Statics: Two Treatises on the Graphical Calculus and Reciprocal Figures in Graphical Statics...*, Clarendon Press, Oxford **1890**.
- [49] P. P. C. V. Block, Ph.D. thesis, Massachusetts Institute of Technology **2009**.
- [50] M. Akbarzadeh, T. Van Mele, P. Block, presented at the *Proc. of the IASS-SLTE Symp. 2014*, (Eds: O. J. B, R. Tarczewski), Brasilia, Brazil **2014**.
- [51] E. Allen, W. Zalewski, *Form and Forces: Designing Efficient, Expressive Structures*, John Wiley & Sons, New York **2009**.
- [52] W. Zalewski, E. Allen, *Shaping Structures: Statics*, Wiley, New York **1998**.
- [53] J. C. Maxwell, *Trans. R. Soc. Edinburgh* **1870**, *26*, 1.
- [54] A. Föppl, *Das Fachwerk im Raume*. Leipzig: Verlag von B.G., Teubner **1892**.
- [55] G. G. Stokes, *Mathematical and Physical Papers*, Cambridge University Press, Cambridge **1905**.
- [56] T. Harboe Nielsen, M. Akbarzadeh, P. Goltermann, in *Proc. of the IASS Annual Symp. 2017, Interfaces: Architecture Engineering Science*, IASS, Madrid, Spain **2017**.
- [57] M. Akbarzadeh, Ph.D. thesis, ETH Zruich, Stefano Franscini Platz 5, Zurich, CH, 8093 **2016**.
- [58] A. McRobie, *Int. J. Space Struct.* **2016**, *31*, 203.
- [59] P. D'acunto, J.-P. Jasienski, P. O. Ohlbrock, C. Fivet, in *Proc. of IASS Annual Symp., Vol. 2017*, International Association for Shell and Spatial Structures (IASS), Madrid, Spain **2017**, pp. 1–10.
- [60] P. O. Ohlbrock, P. D'Acunto, J. P. Jasienski, C. Fivet, in *Proc. of the IASS Annual Symp. 2016 "Spatial Structures in the 21st Century"*, (Eds: K. Kawaguchi, M. Ohsaki, T. Takeuchi), IASS, Madrid, Spain **2016**.
- [61] M. Konstantatou, P. D'Acunto, A. McRobie, *Int. J. Solids Struct.* **2018**, *152*, 272.
- [62] J. Lee, Ph.D. thesis, ETH Zurich, Department of Architecture, Zurich **2018**.
- [63] M. Akbarzadeh, T. Van Mele, P. Block, in *Future Visions*, Proc. of the Int. Association for Shell and Spatial Structures (IASS) Symp. 2015, IASS, Madrid, Spain **2015**.
- [64] M. Akbarzadeh, T. Van Mele, P. Block, in *Future Visions*, Proc. of the Int. Association for Shell and Spatial Structures (IASS) Symp. 2015, IASS, Madrid, Spain **2015**.
- [65] M. Akbarzadeh, T. Van Mele, P. Block, *Comput.-Aided Design* **2015**, *63*, 118.
- [66] M. Hablicsek, M. Akbarzadeh, Y. Guo, *Comput.-Aided Design* **2018**, *108*, 30.
- [67] M. Akbarzadeh, M. Hablicsek, Y. Guo, in *Proc. of the IASS Symp. 2018, Creativity in Structural Design*, MIT, Boston, MA **2018**.
- [68] A. Nejur, M. Akbarzadeh, Polyframe beta: A geometry-based structural form finding plugin for rhinoceros3d, <https://www.food4rhino.com/app/polyframe>, 2018.

- [69] O. Graovac, 3d graphic statics, <https://www.food4rhino.com/app/3d-graphic-statics> **2019**.
- [70] J. Lee, compas 3gs: A 3d graphic statics add-on package for the compas framework, https://github.com/BlockResearchGroup/compas_3gs.
- [71] M. Hablicsek, M. Akbarzadeh, Y. Guo, *Comput.-Aided Design* **2019**, *108*, 30.
- [72] M. Akbarzadeh, M. Hablicsek, *Computer-Aided Design* **2020**, *141*, 103068.
- [73] B. G. Baumgart, in *Proc. of the May 19-22, 1975, National Computer Conf. and Exposition*, Association for Computing Machinery, New York **1975**, pp. 589–596.
- [74] M. Akbari, M. Akbarzadeh, M. Bolhassani, presented at the *Proc. of IASS Symp. 2019 and Structural Membranes 2019, FORM and FORCE*, Barcelona, Spain **2019**.
- [75] D. Young, S. Timoshenko, *Theory of Structures*, McGraw-Hill, New York **1965**.
- [76] M. Akbari, A. Mirabolghasemi, H. Akbarzadeh, M. Akbarzadeh, presented at *ACM Symp. on Computational Fabrication, SCF'20*, Association for Computing Machinery, ACM, Virtual Event, USA **2020**.
- [77] W. Fischer, E. Koch, *Acta Crystallogr. A* **1989**, *45*, 726.
- [78] W. Fischer, E. Koch, *J. Phys. Colloq.* **1990**, *51*, C7C7.
- [79] G. T. Toussaint, C. Verbrugge, C. Wang, B. Zhu, in *Proc. 5th Canadian Conference on Computational Geometry*, Citeseer **1993**.
- [80] N. J. Lennes, *Am. J. Math.* **1911**, *33*, 1/437.
- [81] M. Akbari, Y. Lu, M. Akbarzadeh, in *Proceedings of the Association for Computer-Aided Design in Architecture (ACADIA)*, ACADIA **2021**.
- [82] A. H. Schoen, *Infinite Periodic Minimal Surfaces without Self-intersection*, NASA **1970**.
- [83] H. Karcher, *Manuscripta Mathematica* **1989**, *64*, 291.
- [84] M. Eynbeygui, J. Arghavani, A. Akbarzadeh, R. Naghdabadi, *Acta Mater.* **2020**, *183*, 118.
- [85] J. Shi, A. Akbarzadeh, *Acta Mater.* **2019**, *163*, 91.
- [86] S. J. Hollister, N. Kikuchi, *Computational Mechanics* **1992**, *10*, 73.
- [87] B. Hassani, E. Hinton, *Computers & Structures* **1998**, *69*, 707.
- [88] J. Guedes, N. Kikuchi, *Computer Methods in Applied Mechanics and Engineering* **1990**, *83*, 143.
- [89] G. W. Milton, A. V. Cherkaev, *J. Eng. Mater. Technol.* Oct **1995**, *117*, 483.
- [90] M. Kadic, T. Bückmann, N. Stenger, M. Thiel, M. Wegener, *Appl. Phys. Lett.* **2012**, *100*, 191901.
- [91] Y. Huang, X. Zhang, M. Kadic, G. Liang, *Materials* **2019**, *12*, 3470.
- [92] T. Bückmann, M. Thiel, M. Kadic, R. Schittny, M. Wegener, *Nat. Commun.* **2014**, *5*, 4130.
- [93] Y. Huang, X. Lu, G. Liang, Z. Xu, *Phys. Lett. A* **2016**, *380*, 1334.
- [94] A. Amendola, C. Smith, R. Goodall, F. Auricchio, L. Feo, G. Benzoni, F. Fraternali, *Compos. Struct.* **2016**, *142*, 254.
- [95] D. W. Yee, M. D. Schulz, R. H. Grubbs, J. R. Greer, *Adv. Mater.* **2017**, *29*, 1605293.